ORIGINAL ARTICLE

Model based diagnostic tool for detection of gear tooth crack in a wind turbine gearbox under constant load

Rishi Kumar[1] · Sankar Kumar Roy[1]

Abstract Dynamic modelling of wind turbine drive-train system (WTDS) is important to analyse the behaviour of the vibration and load sharing characteristics of the gearbox. The WTDS mostly contains one planetary gear stage and two parallel gear stages. Sun gear is a significant component in the planetary gear stage and is prone to fail under fatigue loading due to the bending and shear effect. Crack is most likely to occur in the gear tooth root and it decreases the tooth thickness and load-carrying capacity of the gear. The presence of crack decreases the tooth contact number and tooth contact position during the time of meshing. This leads to a variation and quantified reduction in the time varying mesh stiffness (TVMS) of a meshing gear pair. Hence, a dynamic model is developed by including different crack depth levels in the sun gear. The governing equations for the model are derived using Lagrange's formulation and dynamic responses are obtained numerically by step-by-step direct integration method. The dynamic responses like contact forces and angular velocities are estimated at 0%, 10%, and 30% of crack depth in the sun gear tooth and analysed to study the dynamic behaviour of the drive-train for un-cracked and cracked gears beforehand.

1 Introduction

To meet the ever-growing energy requirement, it is essential to look for a renewable source of energy. As of today, the total installed capacity of renewable energy in the world is more than 2500 GW, and in India, it is more than 134 GW (IRENA 2021). Among these renewable energy sources, wind energy alone contributes around 26 percent of the world's generation (IRENA 2021). In India, the generation of wind energy (WE) is around 38.62 GW, which is more than 28 percent of the country's generation from renewable sources (MNRE-GOI 2021). Despite many advantages, the wind turbine (WT) faces many problems like weather extremes, stochastic wind load, thermal cycling, etc. Besides these, the mechanical failure of the bearings, excessive vibration, voltage irregularities, and the failure of the gearbox can reduce the productivity of the whole unit. This leads to a huge impact on the wind energy industry like increase in operation and maintenance cost, power cost, decrease in reliability of the WT. There are various components in a WT. Among these, the gear drive train is one of the vital components of the WT. It increases the rotational speed of the shaft, as required by the generator (Gasch and Twele 2011). Installing the gear drive train reduces the weight and cost of the wind turbine (Helsen et al. 2011). As it is one of the critical components of WT, therefore, it needs proper attention for the smooth functioning of the system. For this, condition monitoring is

✉ Sankar Kumar Roy
   sankar.roy@nitp.ac.in

   Rishi Kumar
   rishi.me15@nitp.ac.in

1 Mechanical Engineering Department, National Institute of
   Technology Patna, Patna, Bihar 800005, India

required to avoid the sudden failure of the gear train in the wind turbine (Singh et al. 2015; Bhattacharya et al. 2014).

In the last decade, many researchers have developed various models related to the WT and its components. Three different multi-body models of wind turbine drive-train system (WTDS) were proposed by the researchers (Peeters et al. 2006). In these models, the drive train contains two planetary gearboxes and one parallel gearbox. The first model is a purely torsional model with a single degree of freedom of each component. The second model is a rigid multi-body model with six degrees of freedom of each component. The third model extended the rigid multi-body model into a flexible multi-body model. Eigen frequencies and Eigenmodes are calculated and compared with the first two models. Later on, the flexible multi-body model was refined to estimate elastic deformation and stress of drive-train components (Peeters et al. 2006). Further, a torsional model of WTDS was investigated (Todorov et al. 2009); in which one planetary gearbox and two parallel gearboxes are used for the drive-train. The model studied the characteristics of the torsional vibrations in the frequency domain. The effect of gear meshes and support bearings on the dynamics of the WT gearbox was studied using a flexible multi-body model (Qin et al. 2009). Further, Helsen et al. (2011) explored the modal behaviour of the drivetrain system by developing a fully flexible model. The non-linear effect of backlash and gear mesh stiffness on internal error excitation in WTDS was also studied by Wang et al. (2011). Xing and Moan (2013) explored the effect of subcomponents mated to the planet carrier by multi-body modelling. Girsang et al. (2014) combined the computer-aided engineering (CAE) tool with MATLAB to study the dynamics of the drive train under different wind load conditions. Shi et al. (2013) investigated the torsional motion by developing a multi-body model of WTDS under constant input torque. The model is developed using Fourier series-based time-varying mesh stiffness (TVMS) and upon numerical simulation, the contact forces are analysed in the frequency domain. It shows that gear mesh frequency (GMF) with sidebands and their harmonics are excited in the frequency domain. Shi et al. (2014) remodelled the previous model into a three-dimensional model for the torsional and translational motion by considering flexibility in gear mesh, shaft, and bearing support. The paper explored the transient response. Initially, Srikanth and Sekhar (2013) studied the dynamics of the WT gearbox by modelling the wind load using an empirical approach. Later on, a dynamic model was investigated in three dimensions with stochastic wind load (Srikanth and Sekhar 2015). The estimated contact forces were analysed in the frequency domain. Zhu et al. (2014) proposed a dynamic model of the WTDS with megawatt capacity to study the vibration and torque responses. The responses showed that the mesh frequencies and their harmonics of the intermediate and high stages were excited. The dynamic response of the power drive train of the wind turbine was analysed during start-up and stop conditions (Viadero et al. 2014). Zhai et al. (2016) studied the effect of assembly error in the wind turbine model. Tan et al. (2019a; b) investigated the effect of electromagnetic stiffness and platform motion on the dynamic response of the wind turbine gearbox in successive articles. Recently, Dewangan et al. (2022) studied the amplitude modulation effect due to carrier rotation and gravity excitation effect on wind turbine gearbox with two-stage planetary gearboxes and one parallel gearbox. Earlier studies are mostly focused on the characteristics of WTDS under healthy conditions. However, there is a possibility of occurring defects like gear tooth wear, crack in gear tooth, etc., which may develop in the WTDS during its operation.

Most of the gearbox crack-related works are done either on parallel or planetary gearbox. Howard et al. (2001) studied the dynamic response of spur gear pair in presence of gear tooth crack. Chen and Shao (2011) proposed a spur gear system. The model studied the effect of tooth crack propagation on the gear dynamics by incorporating tooth crack. Sidebands around the GMF due to gear tooth crack are observed in the frequency domain and they indicate the significance of sidebands for the gear condition monitoring. Chaari et al. (2006) analytically derived the gear mesh stiffness and modelled the planetary gear with sun gear tooth crack to study the dynamic response. Chen and Shao (2013) also proposed a planetary gear model to investigate the effect of crack on dynamic behaviour. Here, the tooth crack is incorporated in sun gear and planet gear separately. The vibration responses are analysed in the frequency domain in which GMF and its harmonics with sidebands are excited. Further, Chen and Shao (2013) analysed the tooth crack in the ring gear. Different sidebands pattern was presented (Hong et al. 2014) in the presence of faults in the planetary gearbox. The paper also revealed that an additional frequency appears in presence of sun gear and planet gear fault. Recently, a nonlinear planetary gear model was proposed (Liu et al. 2017); in which, they investigated the dynamic responses for healthy and faulty conditions in sun gear. They modelled TVMS with and without tooth crack. The fault frequency, sidebands around the gear mesh frequency, and its harmonics are excited in the frequency domain. Ma et al. (2015) reviewed various pieces of literature regarding the dynamics of the cracked gear systems, in which the focus is given on the planetary system. Dewangan et al. (2020) modelled the WT gearbox with a damaged planetary gearbox and detected the damage using modal strain energy and damage index.
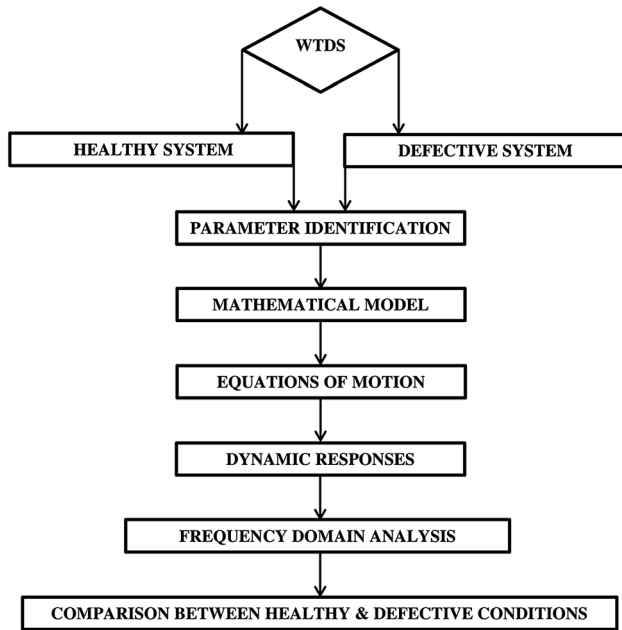
Fig. 1 Flow chart of research methodology

Table 1 Geometrical parameters of lumped masses and gear mesh frequencies of meshing gears

Parameters	Base circle radius, R (mm)	Moment of inertia, (kg-m^2)	Gear mesh frequency, (Hz)
Components			
Rotor, (rot)	–	4.18e06	–
Carrier, (c)	270	57.72	–
Ring, (r)	430	–	25.2
Planet, (p)	160	1.12	25.2
Sun gear, (s)	110	0.86	25.2
Gear 1, (g1)	290	14.32	83.8
Gear 2, (g2)	95	1.515	83.8
Gear 3, (g3)	185	0.105	326.5
Gear 4, (g4)	80	0.2	326.5
Generator, (gen)	–	93.22	–

Apart from the dynamic modelling, researchers also measured and analysed the dynamic responses from the wind turbine gearbox. Lei et al. (2014) reviewed many kinds of literature related to planetary gearbox condition monitoring. The vibration features of a planetary gearbox with healthy and cracked gear tooth were investigated (Liang et al. 2015). Further, they added that the sun gear in the planetary system is more prone to fail while in operation due to its geometrical configuration and gear dynamics. The planetary gear train plays a vital role in WTDS in producing the much-needed high speed at the generator shaft. Yoon et al. (2016) proposed a spectral averaging technique to diagnose the tooth crack in the sun gear, planet gear, and tooth breakage in the ring gear in the planetary gearbox. Chen and Feng (2016) detected the sun gear tooth crack by combining the iterative demodulation technique and the time–frequency domain technique. Wang et al. (2017) had taken the planetary gearbox of the wind turbine to investigate the faults in the ring gear using the frequency spectrum. He et al. (2017) analysed the wind turbine system based on vibration signals and point out the
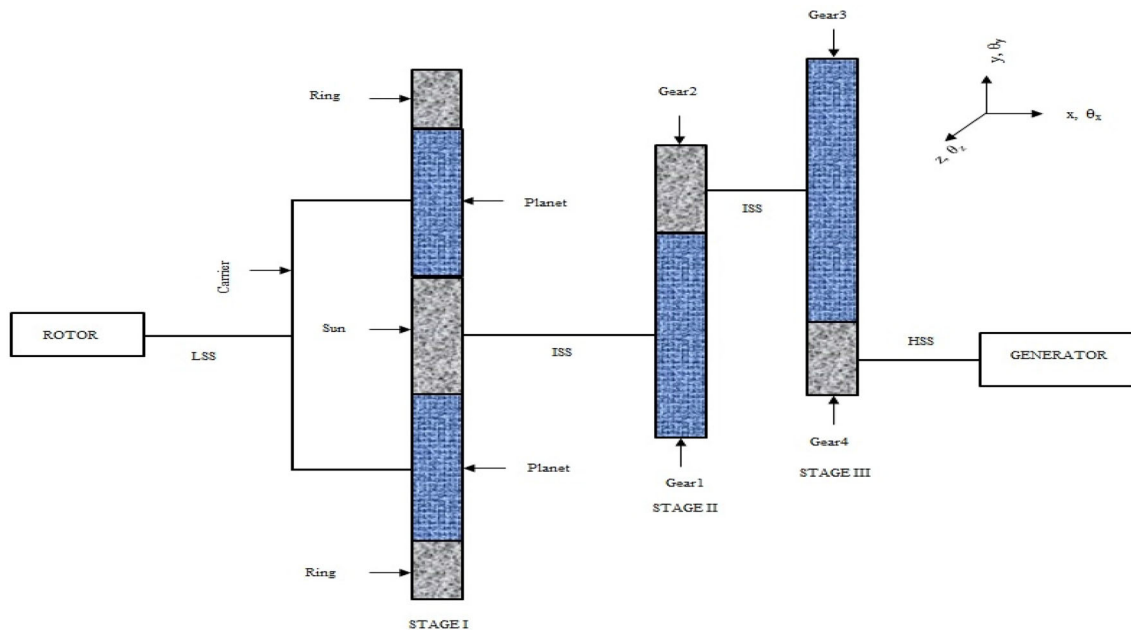

Fig. 2 Line diagram of WTDS

Table 2 Stiffness and material properties of drivetrain components

Parameters	Torsional stiffness, N-m/rad	Mean stiffness, N-m	Bearing stiffness, N-m
Components			
LSS (rotor and carrier)	7.19e7	–	–
ISS (sun and gear 1)	1.4e7	–	–
ISS (gear 2 and gear 3)	1.4e7	–	–
HSS(gear 4 and generator)	0.15e7	–	–
Carrier,k_{bc}	–	–	7.19e7
Sun gear,k_{bs}	–	–	1.4e7
Ring-planet mesh	–	6.3477e9	–
Sun-planet mesh	–	4.6971e9	–
Gear 1-gear 2 mesh	–	4.9349e9	–
Gear 3-gear 4 mesh	–	6.3851e9	–
Pressure angle,$A = pi/9 rad$			
Young's modulus,$E = 206e9 N/m^2$			
Poisson's ratio,$v = 0.3$			
Face width of gear tooth,$L = 11 * module$			
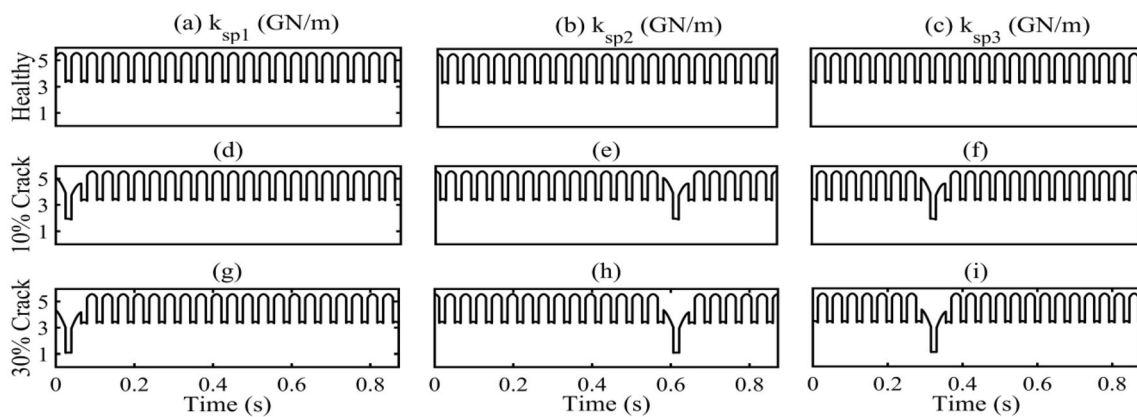
Fig. 3 TVMS for one revolution of sun gear meshing simultaneously with planet1, planet2, and planet3 for healthy **a–c** and defective cases **d–i** including phase shift
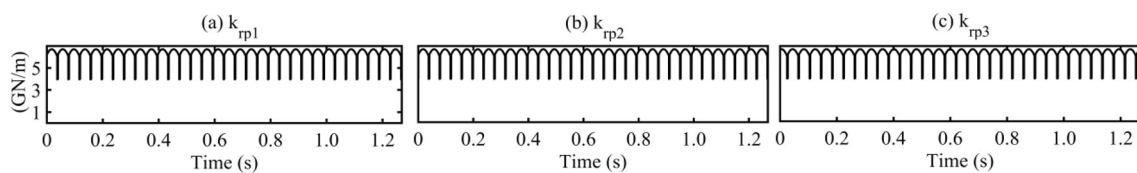

Fig. 4 TVMS for one revolution of planet gear meshing with fixed ring gear: **a** ring-planet1 **b** ring-planet2 **c** ring-planet3
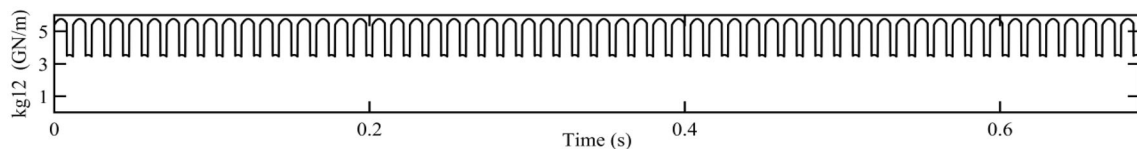
Fig. 5 TVMS for one revolution of gear1 meshing with gear2

excitation of gear mesh frequency and its harmonics. Asymmetric modulation sidebands are also noticed due to mesh phasing of planet gears. Faults in the sun gear of a planetary gearbox were investigated using the optimal demodulation sub-band selection method (Wang et al. 2018). Liu et al. (2018) investigated the planetary gearbox
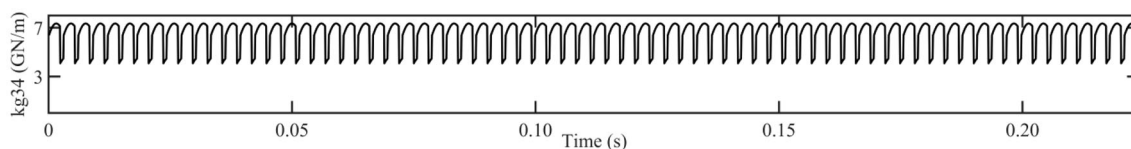
Fig. 6 TVMS for one revolution of gear3 meshing with gear4

having incipient tooth crack in the sun gear. Wang et al. (2019) reviewed the condition monitoring and fault diagnosis aspects of WTDS. Cao et al. (2019) used a bi-directional long short-term memory network to detect sun gear crack in WTDS. Feng et al. (2019) separated harmonic components from the vibration signal using the Vold-Kalman filter and represented in the time–frequency domain to detect the sun gear wear and crack in the planetary gearbox of the WT. According to the literature review, the sun gear of a planetary gearbox is most likely to fail (Lei et al. 2014; Liang et al. 2015) due to its geometrical configuration.

There is very little work (Dewangan et al. 2020) has been done on WTDS modelling by incorporating gear tooth crack. Moreover, researchers have modelled the WTDS using Fourier series-based mesh stiffness (Shi et al. 2013, 2014; Srikanth and Sekhar 2013, 2015, 2016; Zhu et al. 2014) without incorporating the mesh phasing. Fourier series-based mesh stiffness has ignored the effect of changing positions of the gear tooth and excitation of redundant frequency components.

The main objective of this paper is to study the dynamic responses of WTDS under constant wind load. Therefore, a mathematical model has been developed for healthy and defective WTDS. Two defective WTDSs have been modelled by incorporating tooth crack with different depths on the root of the sun gear. The different depths of crack are 10%, and 30%, respectively. In this work, the TVMS is estimated by the potential energy method. The equations of motion of the model are numerically solved using the Houbolt discretization technique. Further, dynamic responses (contact forces and angular speeds) are analysed in the frequency domain for healthy and defective systems. Finally, the results are compared among the healthy and two defective WTDS cases to understand the behaviour of healthy and faulty drivetrain systems.

2 Wind turbine drivetrain modelling and simulation

Understanding the gear dynamics of WTDS in presence of defects will play an important role in the area of WTDS monitoring. Time-varying gear mesh stiffness plays a vital role in establishing the true dynamical characteristics of a gear pair or gearbox. The geometrical configuration of the mating gears led to time-varying characteristics in mesh stiffness. So far, the rectangular waveform of TVMS is used in the dynamic analysis of WTDS which is estimated by the Fourier series method (Shi et al. 2013, 2014; Srikanth and Sekhar 2013, 2015, 2016; Zhu et al. 2014). However, this method neglects the effects of change in the contact positions of the meshing gear tooth and generates some unwanted frequency components (Liang et al. 2014). Therefore, it is necessary to look beyond this method to mitigate the demerits and look for other methods (analytical approach) to estimate the stiffness. The angular orientation of multiple planets in the PGT is not uniform and is positioned around the sun gear at some phase angles (Parker and Lin 2004). However, most of the researchers have neglected the phase angle. Therefore, incorporation of phase angle is required to accurately realise the dynamic characteristics of the model. Moreover, in presence of varying crack levels, modelling of the drivetrain system is required which will help in studying the dynamic behaviour of the model. The flow chart of the research methodology undertaken in this paper for the dynamic analysis is given in Fig. 1.

2.1 Drivetrain model

Figure 2 gives a sketch of the rotor, three stages of gearbox along with intermediate shafts and generator. A planetary drive train and two parallel gear trains are simultaneously connected to transmit the power from the rotor to the generator. Only spur gears are assembled in the drivetrain system. The planet carrier of the planetary drive train is connected to the rotor. The ring gear is assumed fixed with the gearbox housing. The sun gear transmits the power to the succeeding stages. Further, the input shaft of the generator is connected from the third stage. Each drive-train component possesses three rotational and three translational DOF's. However, to refrain from complexity, only rotational DOF about the shaft axis is taken for the 11-lumped masses.

Rotational displacements of three planets are considered in the relative coordinate frame to planet carrier (θ_{cp1}, θ_{cp2} and θ_{cp3}). The absolute displacements of planets are θ_{p1}, θ_{p2} and θ_{p3}. Here, θ_{cpi} and θ_{pi} ($i = 1, 2, 3$) are related as:

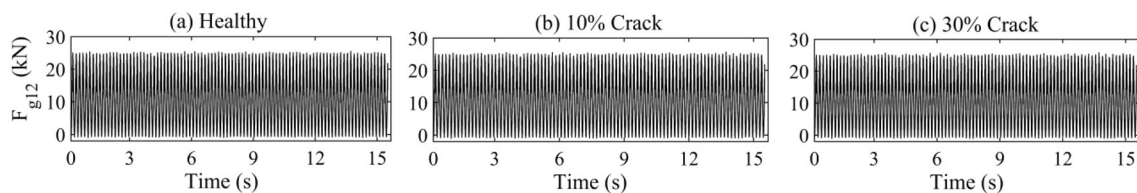$$\theta_{cpi} = \theta_{pi} - \theta_c \tag{1}$$

**Table 3** Values of eigen values and natural frequencies of the proposed model

Eigen value	5.8e8	3.9e8	3.5e8	2.5e8	2.5e8	1.2e8	1.2e7	7.4e6	1.9e6	1.5e3	1.4e1
Frequency (Hz)	3.84e3	3.14e3	2.99e3	2.53e3	2.53e3	1.76e3	572.3	431.7	218.4	6.086	0.603
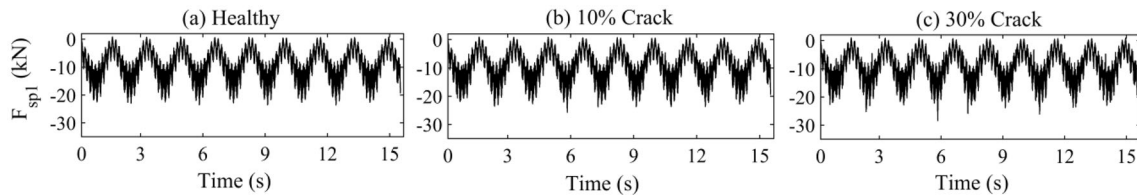
Fig. 7 Contact forces between sun-planet1 at varying tooth root crack levels in the sun gear: **a** healthy, **b** 10% crack, and **c** 30% crack in time domain

Fig. 8 Contact forces between gear1-gear2 at varying tooth root crack levels in the sun gear: **a** healthy, **b** 10% crack, and **c** 30% crack in time domain
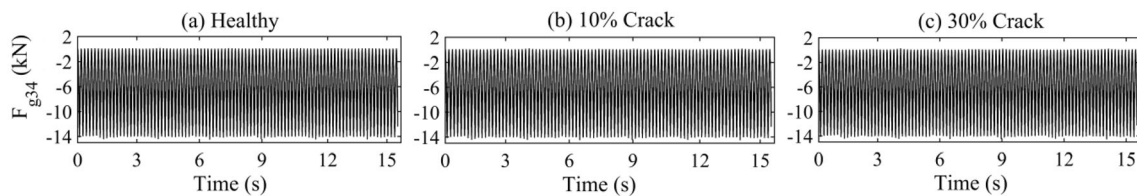
Fig. 9 Contact forces between gear3-gear4 at varying tooth root crack levels in the sun gear: **a** healthy, **b** 10% crack, and **c** 30% crack in time domain

Rotational displacements of drivetrain components namely; rotor, carrier, sun, gear1, gear2, gear3, gear4, and generator are taken in the absolute reference frame, represented by $\theta_{rot}, \theta_c, \theta_s, \theta_{g1}, \theta_{g2}, \theta_{g3}, \theta_{g4}, \theta_{gen}$, respectively. The following relations express the relative displacements (δ) between two meshing gears in the drivetrain:

$$\delta_{spi} = R_s\theta_s - R_c\theta_c + R_p\theta_{pi} \tag{2}$$

$$\delta_{rpi} = -R_c\theta_c - R_p\theta_{pi} \tag{3}$$

$$\delta_{g12} = R_1\theta_{g1} + R_2\theta_{g2} \tag{4}$$

$$\delta_{g34} = R_3\theta_{g3} + R_4\theta_{g4} \tag{5}$$

Here, $\delta_{sp1}, \delta_{sp2} and \delta_{sp3}$ are three displacements when the sun gear is meshing with planet1, planet2, and planet3, respectively. Similarly, for the ring gear meshing internally with the three planets, it is given by $\delta_{rp1}, \delta_{rp2} and \delta_{rp3}$. $\delta_{g12} and \delta_{g34}$ are displacements of the next

two parallel gear drives meshing externally. The radius of the sun gear is R_s and the planet gear is R_p. The radial position of planet carrier from the sun gear centre is:

$$R_c = R_s + R_p \tag{6}$$

Lagrange's equation is given by:

$$\frac{d}{dt}\left(\frac{\partial L}{\partial \dot{\theta}_l}\right) - \frac{\partial L}{\partial \theta_l} = \Gamma_l \tag{7}$$

Here, θ stands for rotational deflection and Γ stands for torque. The subscript 'l' stands for the rotor, carrier, planet1, planet2, planet3, sun, gear1, gear2, gear3, gear4, generator, respectively. Lagrangian 'L' for the system is obtained by:

$$L = T - V \tag{8}$$

$$L = \frac{1}{2} \left\{ \begin{array}{c} J_{rot}\dot{\theta}_{rot}^2 + (J_c + 3mR_c^2)\dot{\theta}_c^2 + J_p\left(\dot{\theta}_{cp1} + \dot{\theta}_c\right)^2 + J_p\left(\dot{\theta}_{cp2} + \dot{\theta}_c\right)^2 + J_p\left(\dot{\theta}_{cp3} + \dot{\theta}_c\right)^2 \\ + J_s\dot{\theta}_s^2 + J_{g1}\dot{\theta}_{g1}^2 + J_{g2}\dot{\theta}_{g2}^2 + J_{g3}\dot{\theta}_{g3}^2 + J_{g4}\dot{\theta}_{g4}^2 + J_{gen}\dot{\theta}_{gen}^2 \end{array} \right\}$$

$$- \frac{1}{2} \left[\begin{array}{c} k_{sp1}\left(R_s\theta_s - R_s\theta_c + R_p\theta_{cp1}\right)^2 + k_{sp2}\left(R_s\theta_s - R_s\theta_c + R_p\theta_{cp2}\right)^2 + k_{sp3}\left(R_s\theta_s - R_s\theta_c + R_p\theta_{cp3}\right)^2 \\ + k_{rp1}\left(R_r\theta_c + R_p\theta_{cp1}\right)^2 + k_{rp2}\left(R_r\theta_c + R_p\theta_{cp2}\right)^2 + k_{rp3}\left(R_r\theta_c + R_p\theta_{cp3}\right)^2 \\ + k_{g12}\left(R_{g1}\theta_{g1} + R_{g2}\theta_{g2}\right)^2 + k_{g34}\left(R_{g3}\theta_{g2} + R_{g4}\theta_{g3}\right)^2 + k_{t1}\left(\theta_c - \theta_{rot}\right)^2 \\ + k_{t2}\left(\theta_{g1} - \theta_s\right)^2 + k_{t2}\left(\theta_{g3} - \theta_{g2}\right)^2 + k_{t3}\left(\theta_{g4} - \theta_{gen}\right)^2 + k_{bc}y\theta_c^2 + k_{bs}\theta_s^2 \end{array} \right] \tag{9}$$

Here, $J_{rot}, J_c, J_s, J_p, J_{g1}, J_{g2}, J_{g3}$ and J_{g4} are the moment of inertia of the rotor, carrier, sun gear, gears 1–4 respectively. k_{spi} and k_{rpi} are the mesh stiffness for the externally meshed sun gear and ith planet and internally meshed ring gear and the ith planet, where $i = 1, 2, 3$. k_{g12} and k_{g34} are the mesh stiffness between the gears 1–2 and gears 3–4. k_{t1}, k_{t2} and k_{t3} are torsional stiffness of connecting shafts; for LSS (low-speed shaft), ISS (intermediate speed shaft), HSS (high-speed shaft) respectively. k_{bc} and k_{bs} are bearing stiffness of the planet carrier and sun gear respectively.

With the help of Lagrange's formulation, the differential equations are obtained and given below in matrix equation:

$$M\ddot{\theta} + K\theta = \Gamma \tag{10}$$

The Mass matrix, M, stiffness matrix, K, displacement vector matrix, θ, and torque vector matrix, Γ, are quoted in the "Appendix". Characteristic rotational frequencies of the drive-train components are estimated using the following relations (Lei et al. 2014).
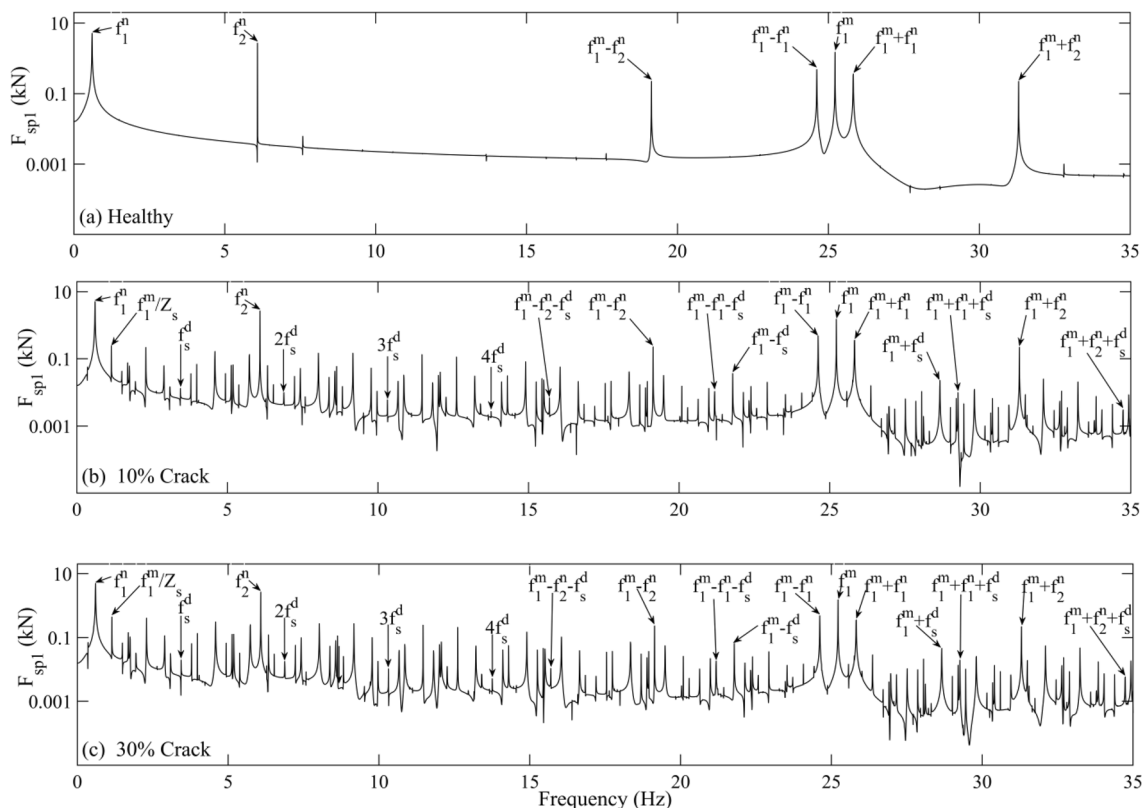
Fig. 10 Frequency spectra of contact forces between sun-planet1 assuming y-axis in logarithmic scale (0–35 Hz): a healthy, b 10% crack, and c 30% crack
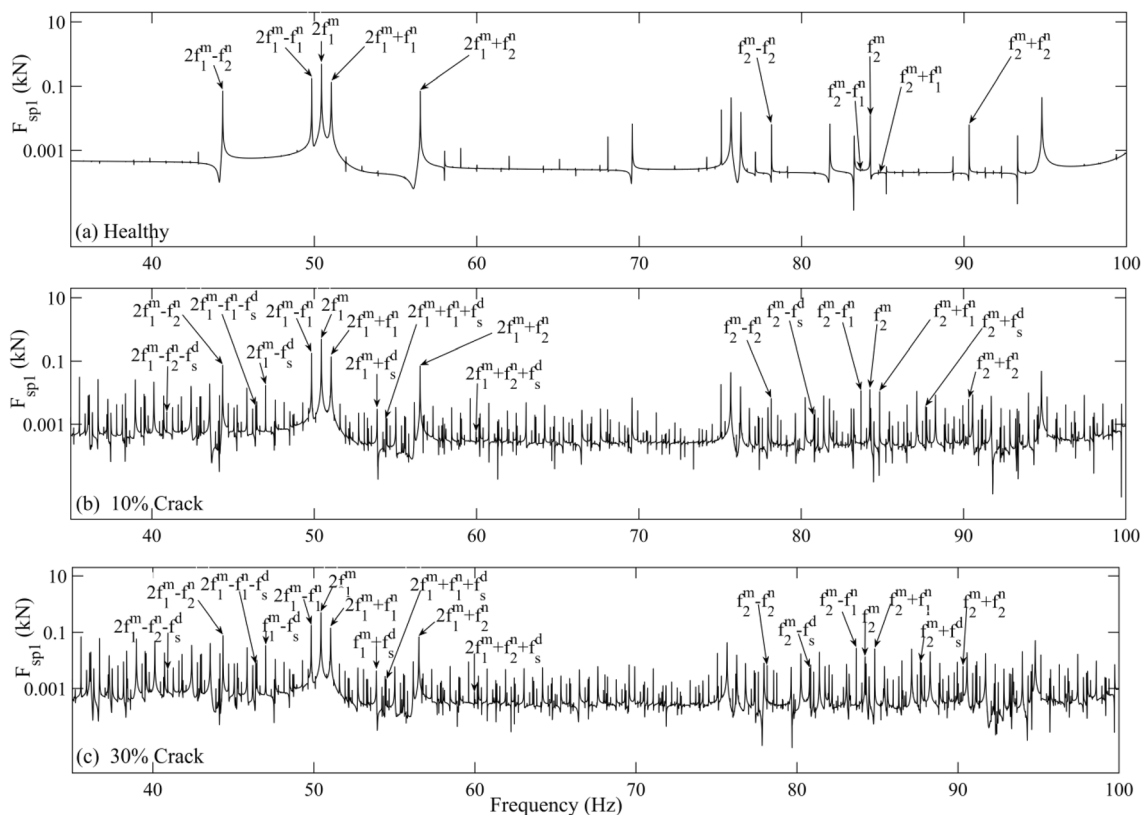
Fig. 11 Frequency spectra of contact forces between sun-planet1 assuming y-axis in logarithmic scale (35–100 Hz): **a** healthy, **b** 10% crack, and **c** 30% crack

$$f_p = f_c \left(1 - \frac{Z_r}{Z_p}\right) \tag{11}$$

$$f_{cp} = f_p - f_c \tag{12}$$

Carrier rotational frequency (f_c) is assumed to be equal to the rotor rotational frequency. Rotational frequency (f_s) of the sun gear is given by,

$$f_s = f_c \left(1 + \frac{Z_r}{Z_s}\right) \tag{13}$$

where Z_s, Z_r, Z_p stand for teeth number in the sun, ring, and planet gear, respectively.

For the second stage, the rotational frequency (f_{g2}) of the pinion is (f_{g1}) as

$$f_{g2} = f_{g1} \left(\frac{Z_{g1}}{Z_{g2}}\right) \tag{14}$$

For the third stage, the rotational frequency (f_{g4}) of the pinion (f_{g3}) as

$$f_{g4} = f_{g3} \left(\frac{Z_{g3}}{Z_{g4}}\right) \tag{15}$$

The Z_{g1}, Z_{g2}, Z_{g3}, and Z_{g4} are the number of teeth in parallel gears of the 2nd and 3rd stage of the WTDS. The

time period between sun-planet (ith) and ring-planet (ith) mesh pair is given by:

$$T = \frac{2\pi}{f_1^m Z_p} \tag{16}$$

where f_1^m represents the GMF for the planetary gear train, can be expressed as:

$$f_1^m = f_s \frac{Z_r Z_s}{Z_r + Z_s} \tag{17}$$

GMF of the 2nd stage (f_2^m) is:

$$f_2^m = f_{g1} Z_{g1} = f_{g2} Z_{g2} \tag{18}$$
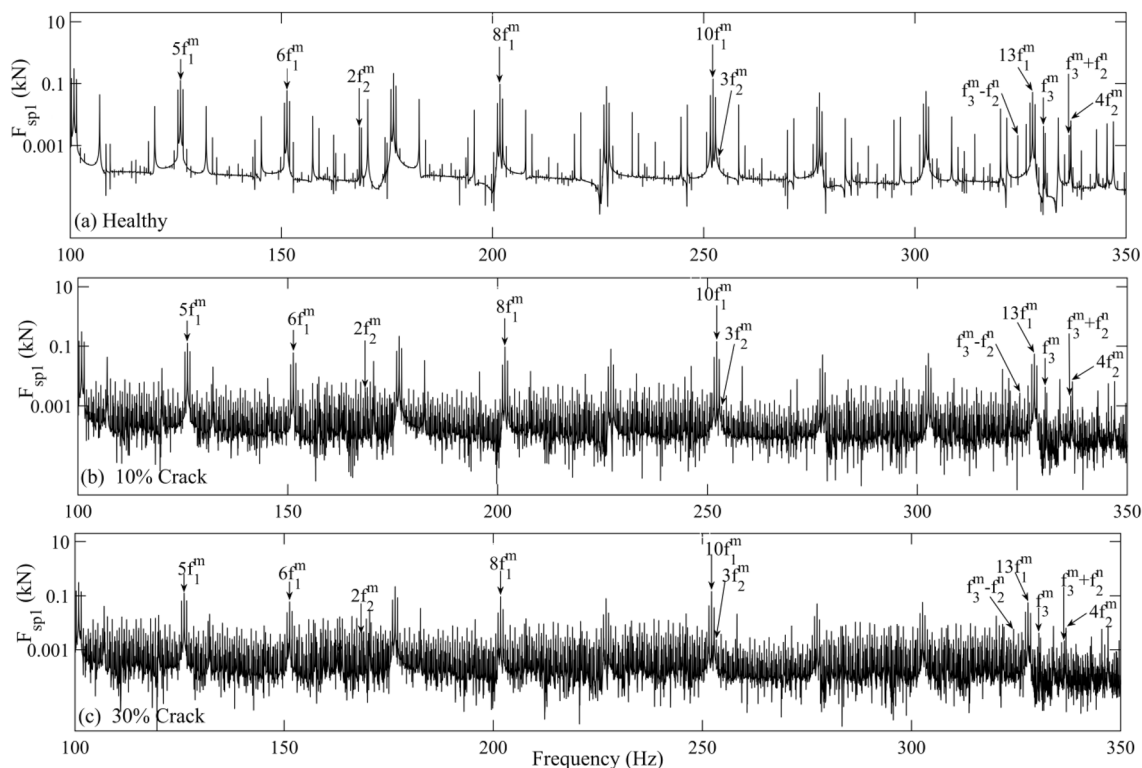
GMF of the 3rd stage (f_3^m) is:

$$f_3^m = f_{g3} Z_{g3} = f_{g4} Z_{g4} \tag{19}$$

In presence of a fault in planetary gear, the fault characteristic frequency (f_s^d) is excited, which is given by (Chaari et al. 2006),

$$f_s^d = \frac{f_1^m}{Z_s} n \tag{20}$$

where the number of planets is n in the planetary gear train of WTDS.

Fig. 12 Frequency spectra of contact forces between sun-planet1 assuming y-axis in logarithmic scale (100–350 Hz): **a** healthy, **b** 10% crack, and **c** 30% crack

2.2 Gear mesh stiffness estimation

The angular orientation of the ith planet (i stands for 1, 2, and 3) with respect to the sun gear is represented by an angle psi (ψ_i).

$$\psi_i = \frac{2\pi(i-1)}{n} \tag{21}$$

Tooth meshing between two gears (either external or internal) is modelled using a spring. Stiffness of gear tooth meshing can be computed by Fourier series approximation (Shi et al. 2013, 2014; Srikanth and Sekhar 2013, 2015, 2016; Zhu et al. 2014), finite element method (Wang and Howard 2004), analytical method (Liang et al. 2014; Chaari et al. 2009), experimental method (Pandya et al. 2013; Raghuwanshi et al. 2016). Contrary to the shortcomings associated with the other methods, the potential energy method is simple and is derived theoretically (Liang et al. 2014; Chaari et al. 2009). Hence, the analytical method is used in the estimation of the mesh stiffness of the system. The relationship of mesh stiffness (k) for external-external or external-internal gear pair is given by:

$$k = \sum_{j=1}^{2} \frac{1}{\frac{1}{k_{b1,j}} + \frac{1}{k_{s1,j}} + \frac{1}{k_{a1,j}} + \frac{1}{k_{h,j}} + \frac{1}{k_{b2,j}} + \frac{1}{k_{s2,j}} + \frac{1}{k_{a2,j}}} \tag{22}$$

Here, bending stiffness is given by k_b. k_s gives shear stiffness and axial compressive stiffness is given by k_a. k_h represents the Hertzian stiffness. j stands either for first tooth ($j = 1$) or second tooth ($j = 2$) when the contact ratio is greater than one. The individual involute tooth profile of the meshing gears is regarded as a cantilever beam protruding from the root circle of gears. The bending, shear, and axial compressive stiffness are put in the MatLab coding with various boundary conditions of the cantilever beam. The gear parameters given in Tables 1 and 2 are used in the simulation. The Hertzian stiffness is separately estimated for the two curved surfaces of tooth meshing. Finally, the mesh stiffness for one mesh cycle is obtained. The mesh phasing in the planetary gear drive leads to the angular shifting of data points of mesh stiffness in a mesh cycle. The mesh phase angles for the ith planet meshing either with the sun gear or with the ring gear are:

$$\gamma_{spi} = \pm \psi_i \frac{Z_s}{2\pi} \tag{23}$$

$$\gamma_{rpi} = \mp \psi_i \frac{Z_r}{2\pi} \tag{24}$$
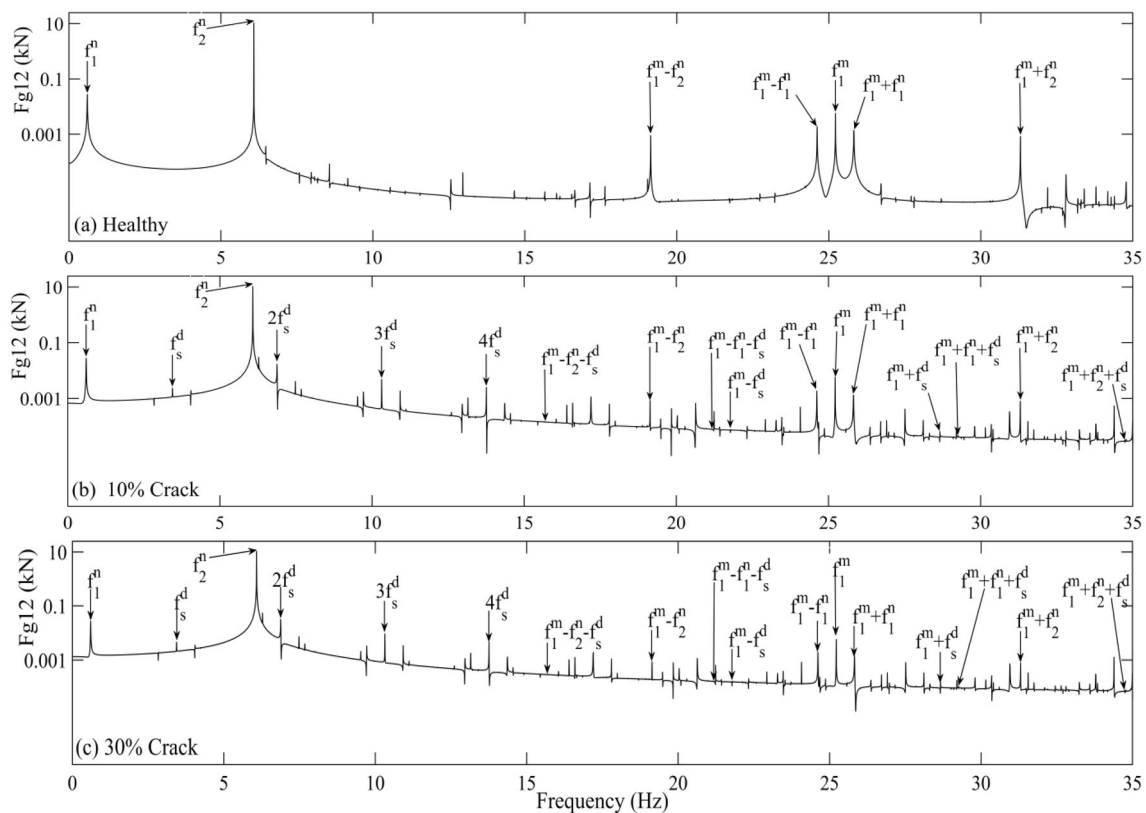
Fig. 13 Frequency spectra of contact forces between gears1-gear2 assuming y-axis in logarithmic scale (0–35 Hz): **a** healthy, **b** 10% crack, and **c** 30% crack

The phase angle of the ith planet to the sun gear is γ_{spi} and γ_{rpi} is the phase angle of the ith planet to the ring gear. The value obtained by the above two Eqs. (23) and (24) can have integral and fractional values. The fractional part is quantitatively used to shift the data points of mesh stiffness in one mesh cycle and the integral part is used to shift the whole mesh cycle in one specific revolution of the sun gear. The relative mesh phasing between the sun gear and ring gear meshing with the ith planet is indicated by γ_{rs}. The value of γ_{rs} is calculated in the MatLab software for the given parameters (Parker and Lin 2004). The value of γ_{rs} is identical for each meshing pair in the planetary gear drive. The TVMSs of the ith planet by incorporating mesh phase angle are:

$$k_{spi} = k(t - \gamma_{spi}T) \tag{25}$$

$$k_{rpi} = k(t - \gamma_{rpi}T - \gamma_{rs}T) \tag{26}$$

where k is the stiffness estimated from the Eq. (22). T is the time period of one mesh cycle and t is the instantaneous time during the meshing. In presence of crack, the quantitative value of bending and shear stress gets reduced due to the reduction in tooth cross-sectional area. This led to a quantified reduction in the TVMS of the planet-sun gear meshing for varying crack levels in the sun gear tooth.

With the increase in the crack surface area, there is more reduction in stiffness value. The subplots in Fig. 3 are showing different mesh stiffness for healthy sun gear, 10%, and 30% crack level with three different planets and phase shift. The mesh stiffness between the ith planet and the sun gear is represented by k_{spi}; (k_{sp1}, k_{sp2}, k_{sp3}).

The subplots in Fig. 4 are representing the stiffness of the ring gear and three planet gears under meshing. The effect of mesh phasing due to one revolution of planet gear is also shown. TVMS for ring gear and the ith planet is represented by k_{rpi}; (k_{rp1}, k_{rp2}, k_{rp3}).

Figures 5 and 6 show the gear mesh stiffness of the second stage; k_{g12} and third stage; k_{g34} of the drivetrain system, respectively. The diagrams are showing the stiffness data points for one revolution of driver gears of respective stages.

2.3 Numerical analysis

When the direct integration method in the closed-form fails to produce the results, an implicit numerical integration method is applied to the model. An approximate solution obtained by the numerical techniques need not satisfy the differential equations of a model continuously at all-time t rather at some discrete time interval $i\Delta t$, where i ranges
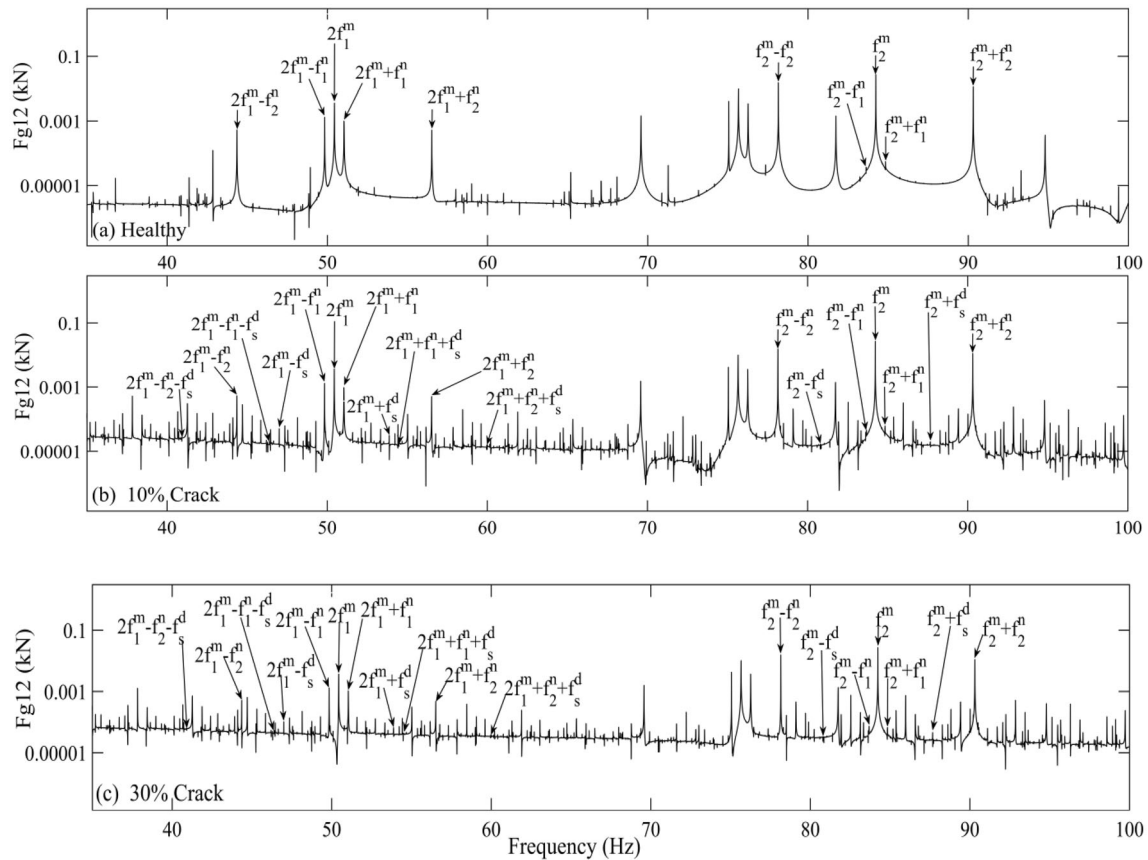
Fig. 14 Frequency spectra of contact forces between gears1-gear2 assuming y-axis in logarithmic scale (35–100 Hz): a healthy, b 10% crack, and c 30% crack

from 0 to $T/\Delta t$. T is the time duration for which the numerical integration is done. Δt is the critical time step of numerical integration (Rao 2011). The drive-train model discussed here is numerically solved using the Houbolt method to obtain the steady-state response. With the help of Taylor's series, equations that co-relate the displacement (θ), velocity ($\dot{\theta}$), and acceleration ($\ddot{\theta}$) terms are given below as:

$$\dot{\theta}_{i+1} = \frac{1}{6\Delta t}(11\theta_{i+1} - 18\theta_i + 9\theta_{i-1} - 2\theta_{i-2}) \quad (27)$$

$$\ddot{\theta}_{i+1} = \frac{1}{(\Delta t)^2}(2\theta_{i+1} - 5\theta_i + 4\theta_{i-1} - \theta_{i-2}) \quad (28)$$

In the central difference method, the displacement (θ), velocity ($\dot{\theta}$), and acceleration ($\ddot{\theta}$) are related by the following equations:

$$\dot{\theta}_{i+1} = \frac{1}{2\Delta t}(\theta_{i+1} - \theta_{i-1}) \quad (29)$$

$$\ddot{\theta}_{i+1} = \frac{1}{(\Delta t)^2}(\theta_{i+1} - 2\theta_i + \theta_{i-1}) \quad (30)$$

The equations of motion for the WTDS, when put into matrix form are written as:

$$M\ddot{\theta}_{i+1} + K\theta_{i+1} = \Gamma_{i+1} \quad (31)$$

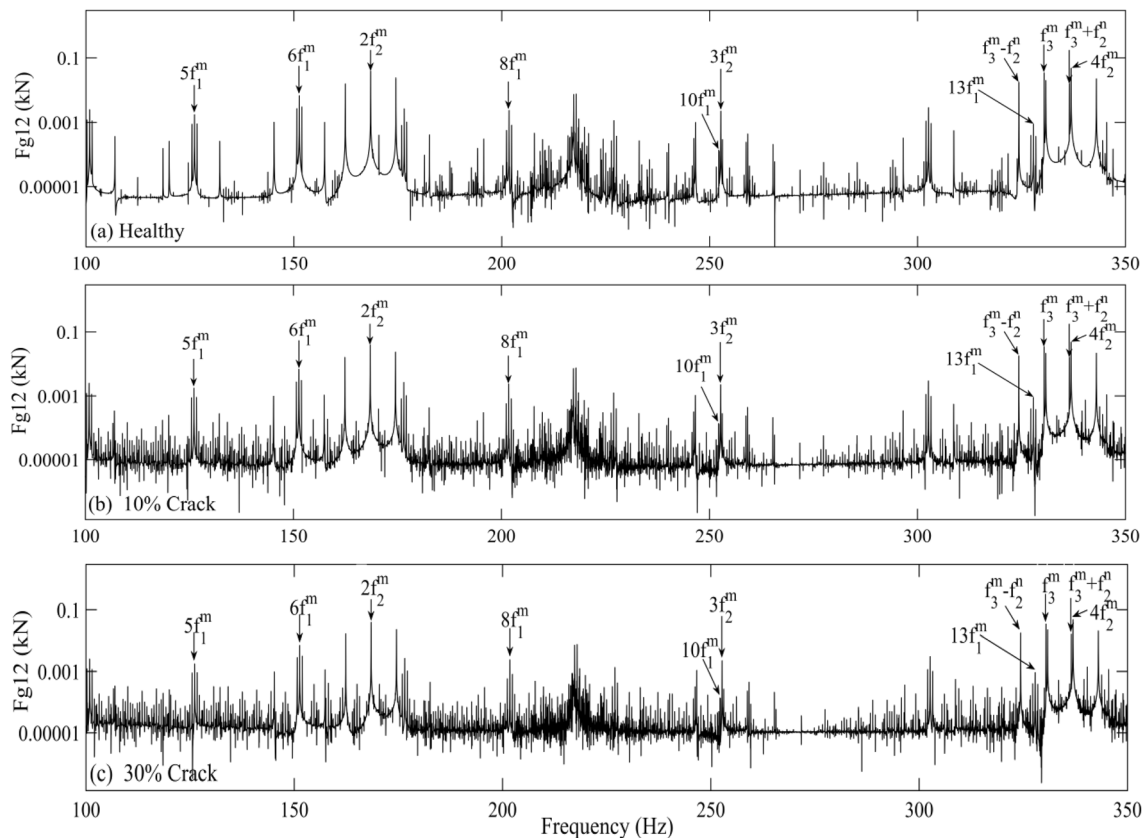The expressions obtained after rearranging the terms in the sequence are given by:

By the Houbolt method,

$$\theta_{i+1} = \left[\frac{2}{(\Delta t)^2}M + K\right]^{-1} * \left\{\Gamma_{i+1} + \left(\frac{5}{(\Delta t)^2}M\right)\theta_i - \left(\frac{4}{(\Delta t)^2}M\right)\theta_{i-1} + \left(\frac{1}{(\Delta t)^2}M\right)\theta_{i-2}\right\} \quad (32)$$

By the central difference method,

$$\theta_{i+1} = \left[\frac{1}{(\Delta t)^2}M\right]^{-1} * \left\{\Gamma_i - \left(K - \frac{2}{(\Delta t)^2}M\right)\theta_i - \left(\frac{1}{(\Delta t)^2}M\right)\theta_{i-1}\right\} \quad (33)$$

At t = 0, acceleration is calculated using Eq. (10) as given as:

Fig. 15 Frequency spectra of contact forces between gears1-gear2 assuming y-axis in logarithmic scale (100–350 Hz): **a** healthy, **b** 10% crack, and **c** 30% crack

$$\ddot{\theta} = M^{-1}(\Gamma - K\theta) \qquad (34)$$

The central difference method is executed for the first two iterations and then the Houbolt method is continued henceforth.

3 Results

The numerical simulation of the mathematical model is done for constant torque in MatLab (Shi et al. 2013). The rotor and generator are not subjected to any external loadings and it is assumed that the rotor is excited with 0.3 Hz of constant rotational frequency. This frequency gives a rotational motion to the gearbox assembly through the planet carrier. Tables 1 and 2 tabulate the drive-train components specification used in the wind turbine model (Todorov et al. 2009). Base circle radius, inertia, and mesh frequency are tabulated in Table 1. Torsional stiffness of the intermediate shaft, bearing stiffness, mean stiffness of meshing gears, Young's modulus, poison's ratio, and pressure angle are given in Table 2. QR-decomposition technique is applied to estimate the Eigen solutions of the system, given in Table 3.

The subplots in Fig. 7 represent the contact forces between planet1 and sun gear for healthy and defective conditions. The subplots in Figs. 8 and 9 show the contact forces of parallel gear trains in three different situations. Figures 10, 11, 12 show the frequency spectra of the contact forces between sun and planet1 for un-cracked and cracked gears with varying crack levels. The spectra show the excitation of 1st and 2nd natural frequencies (f_1^n, f_2^n) of the system, 1st stage GMF (f_1^m) along with sidebands and their harmonics. 1st and 2nd natural frequencies are 0.603 Hz and 6.086 Hz, respectively, which are shown in Table 3. The excitation of 2nd and 3rd stage GMF (f_2^m, f_3^m) and their harmonics with sidebands are also seen in the frequency spectra but with minimal significance. For cracked sun gear, fault frequency (f_s^d) and its harmonics are excited as well as it appears as sidebands around the 1st and 2nd GMFs. Thus it modulates the contact force. The frequency spectrum of the contact force between gear 1 and gear 2 is plotted in Figs. 13, 14, 15. The significant frequencies are earmarked with arrows for healthy and defective gears. Here, first and second natural frequencies; first, second, and third stage GMFs; their harmonics and sidebands are observed. In defective cases, fault frequency and its harmonics appear. Similar to the previous contact

force, the fault frequency also modulates the 1st and 2nd GMFs. The contact force between gear 3 and gear 4 is fast Fourier transformed and obtained frequency spectrum is plotted in Figs. 16, 17, 18. The spectrum highlights the excitation of natural frequencies, mesh frequencies, and their harmonics with sidebands for the healthy case. For the defective cases, the fault frequency and its harmonics also got excited and modulating the mesh frequencies.

In Figs. 19, 20, angular speed fluctuations of the sun gear and gear4 are plotted in the time domain. The time domain representation in Figs. 19, 20 depicts the amplitude variation in different situations but the amplitude variation is very negligible. Hence, the speed fluctuations are fast Fourier transformed to observe the excitation of various frequencies. The frequency spectrum of sun gear is plotted in Figs. 21, 22, 23 for three different situations. For the healthy system, the frequency spectrum shows the excitation of first and second natural frequencies (f_i^n, i = 1, 2), GMFs along with sidebands and their harmonics. The first and second natural frequencies are modulating the GMFs and their harmonics. The sidebands around the first GMF are observed due to amplitude modulation of natural frequencies. However, for the defective cases, the frequency

spectrum shows the excitation of fault characteristic frequency (f_s^d) and its harmonics (Liu et al. 2017; Ma et al. 2015; Lei et al. 2014; Liang et al. 2015; Yoon et al. 2016; Chen et al. 2016; Wang et al. 2017). This fault frequency is modulating the first stage GMF and its harmonics. The modulating features of the first two natural frequencies and fault frequency are observed in the sidebands at $f_1^m \pm f_i^n$ and $f_1^m \pm f_s^d$, which are shown in Figs. 21, 22, 23. The speed fluctuation of gear 4 is analysed in the frequency domain using FFT as shown in Figs. 24, 25, 26. For the healthy case, similar to speed fluctuation of the sun gear, the first two natural frequencies, GMFs, and their harmonics with sidebands are excited. For the defective cases, the fault frequency and its harmonics appear in the spectrum. The amplitude of the fault frequency and its harmonics increase when the depth of crack increases. However, modulating characteristic of the fault frequency is not observed in the speed fluctuation of gear 4.
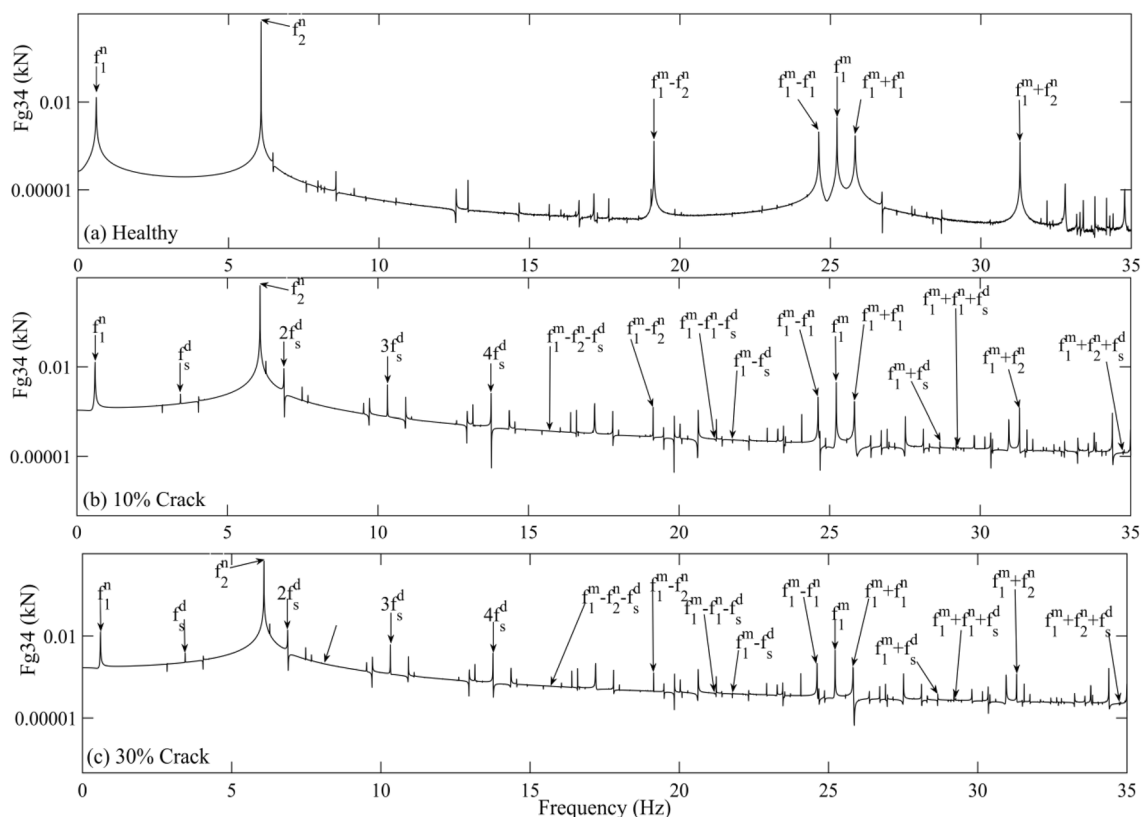
Fig. 16 Frequency spectra of contact forces between gear3-gear4 assuming y-axis in logarithmic scale (0–35 Hz): a healthy, b 10% crack, and c 30% crack
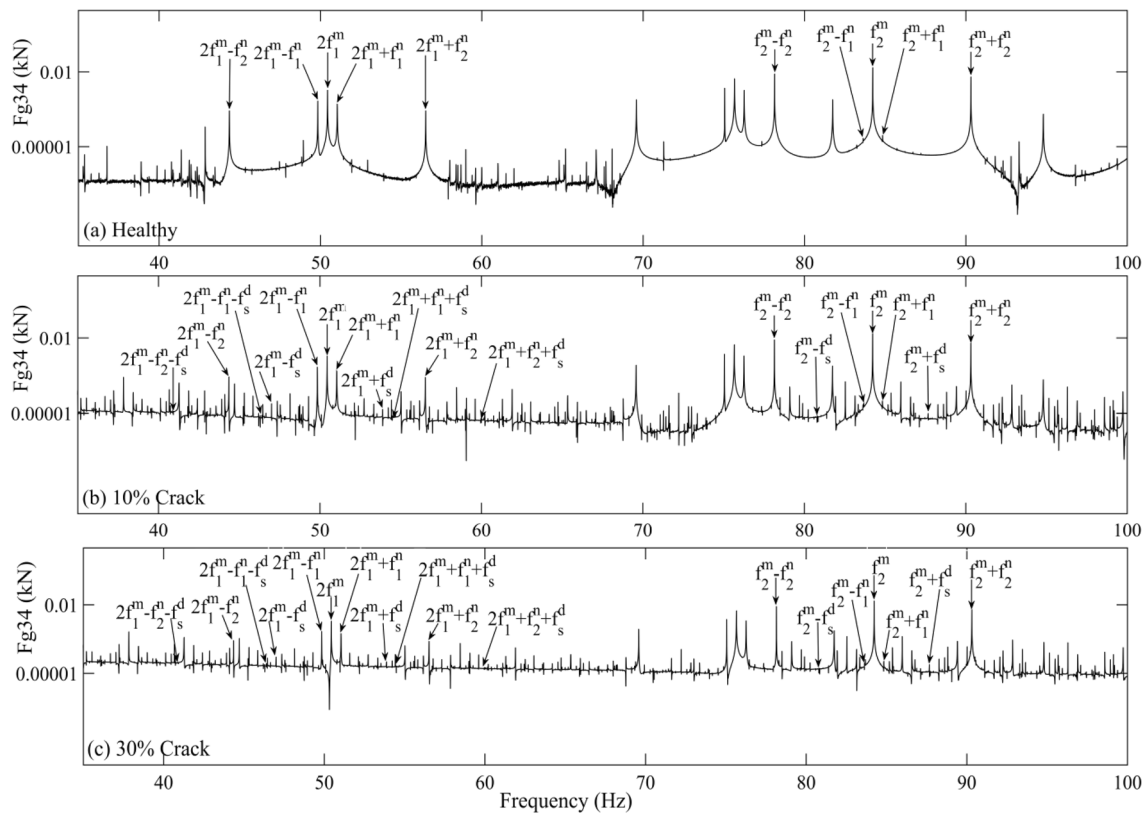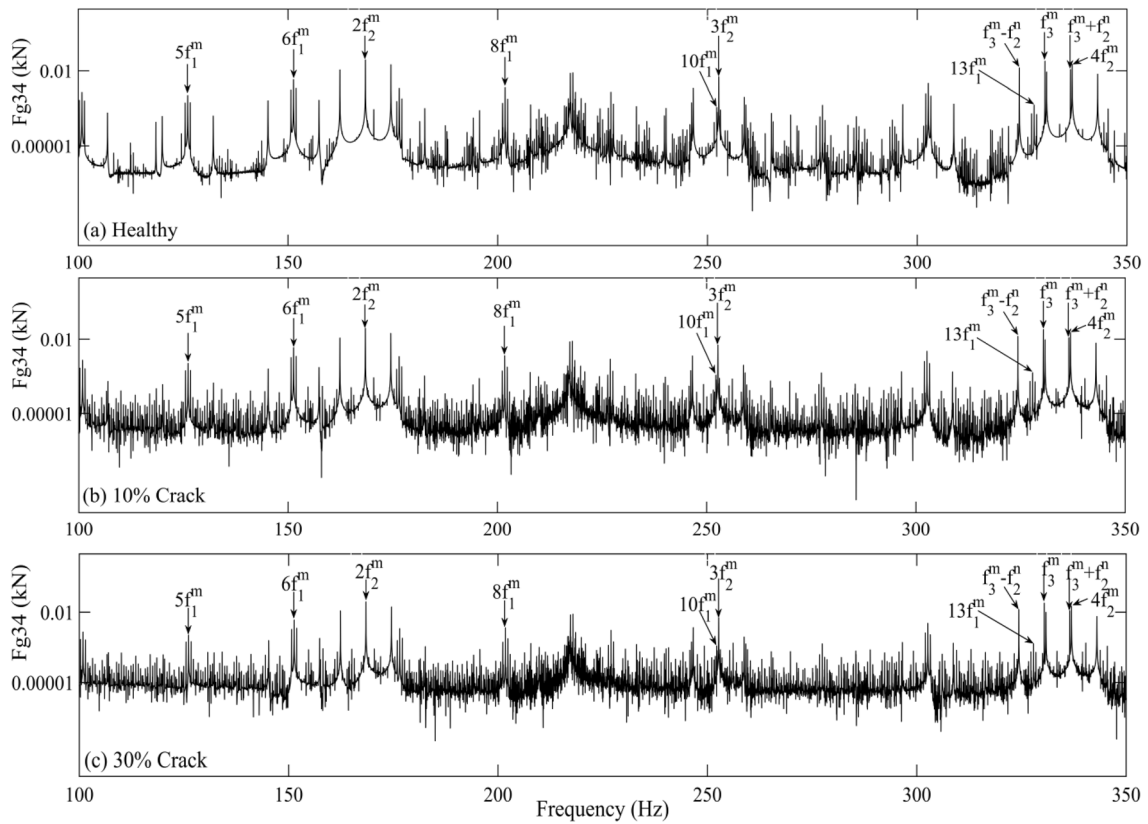
Fig. 17 Frequency spectra of contact forces between gear3-gear4 assuming y-axis in logarithmic scale (35–100 Hz): **a** healthy, **b** 10% crack, and **c** 30% crack

4 Discussion

There are many operational and physical constraints linked to the wind turbine that led to any unforeseen industrial hazard. It can badly affect the operational life and reliability of the wind farms. Therefore, a reliable wind turbine system with a proper health diagnosis system should be developed. Hence, a mathematical model is developed. The Eigen solutions of the system shown in Table 3 are positive values. That indicates the stability of the model (Todorov et al. 2009). It is earlier mentioned that various signals like vibration signal, speed signal, current signal, etc. are used in WT condition monitoring. The vibration signal is mainly acquired from the drivetrain system by an accelerometer and the signal is related to the contact forces. The accelerometer can be installed easily at the respective bearing positions. Hence, the contact forces between sun-planet, gear1-gear2, and gear3-gear4 for the un-cracked and cracked tooth of the sun gear are investigated. In Figs. 7, 8, 9, there is a gradual increase in the mean values of contact forces from un-cracked gears to cracked gears with the increase in the crack levels. Though the mean

values are changing due to gear defect, yet it is not clear to recognise the location of the gear defect.

Therefore, the contact forces are fast Fourier transformed, and amplitude modulation by natural frequency and fault frequency of all GMFs and their harmonics is observed in Figs. 10, 11, 12. The dominance of 1st GMF and its harmonics are observed since the amplitudes of 2nd and 3rd GMF's are lower in the spectrum. The modulating characteristics are observed in the sidebands at $f_l^m \pm f_i^n$, where l can be 1, 2, 3 and i can be 1, 2. However, when a crack is initiated in the sun gear, fault characteristic frequency (f_s^d) and its harmonics are excited (Liu et al. 2017; Ma et al. 2015; Lei et al. 2014; Liang et al. 2015; Yoon et al. 2016; Chen et al. 2016). For the defective system, various sidebands are excited due to the modulation effect of either natural frequency or fault frequency, or both. These modulations are observed at $f_1^m \pm f_i^n$, $f_1^m \pm f_s^d$ and $f_1^m \pm f_i^n \pm f_s^d$ (Liu et al. 2017; Ma et al. 2015; Liang et al. 2015) in frequency spectrum very well.
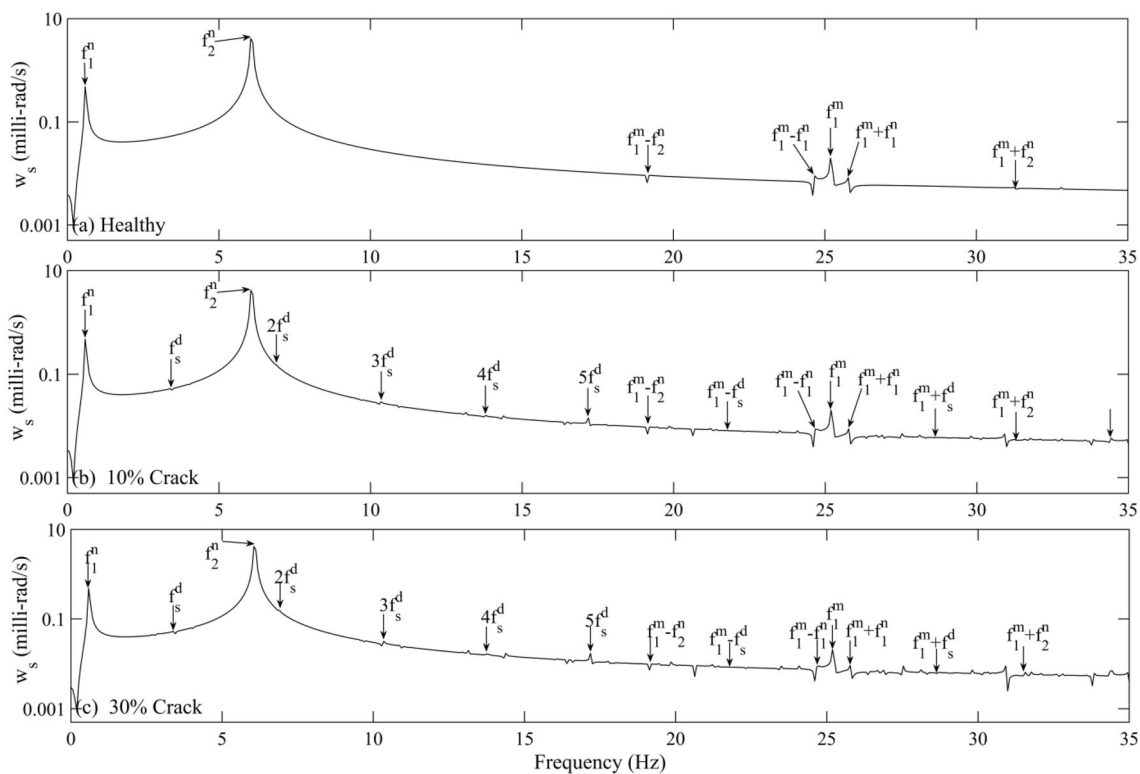
Fig. 18 Frequency spectra of contact forces between gear3-gear4 assuming y-axis in logarithmic scale (100–350 Hz): **a** healthy, **b** 10% crack, and **c** 30% crack
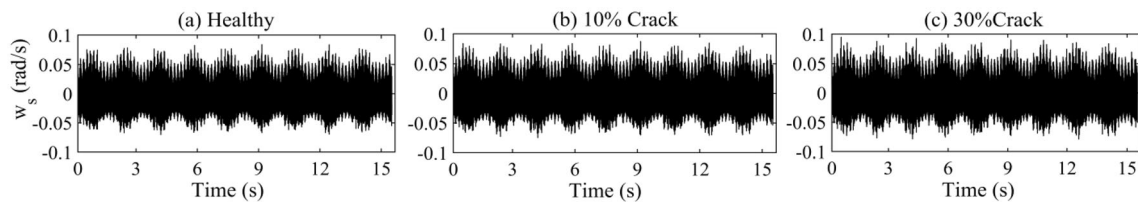

Fig. 19 Time domain representation of angular speed fluctuation of sun gear: **a** healthy, **b** 10% crack, and **c** 30% crack in the tooth root of the sun gear
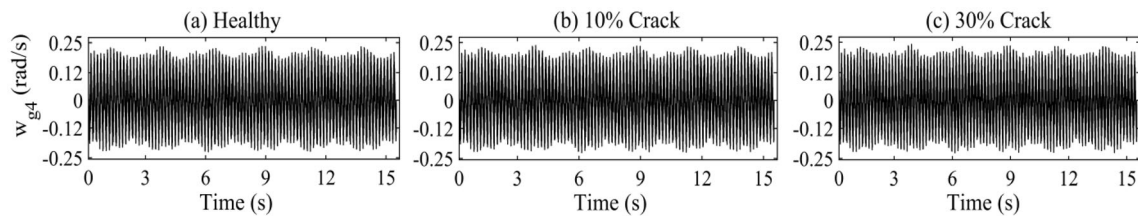
Fig. 20 Time domain representation of angular speed fluctuation of gear4: **a** healthy, **b** 10% crack, and **c** 30% crack in the tooth root of the sun gear
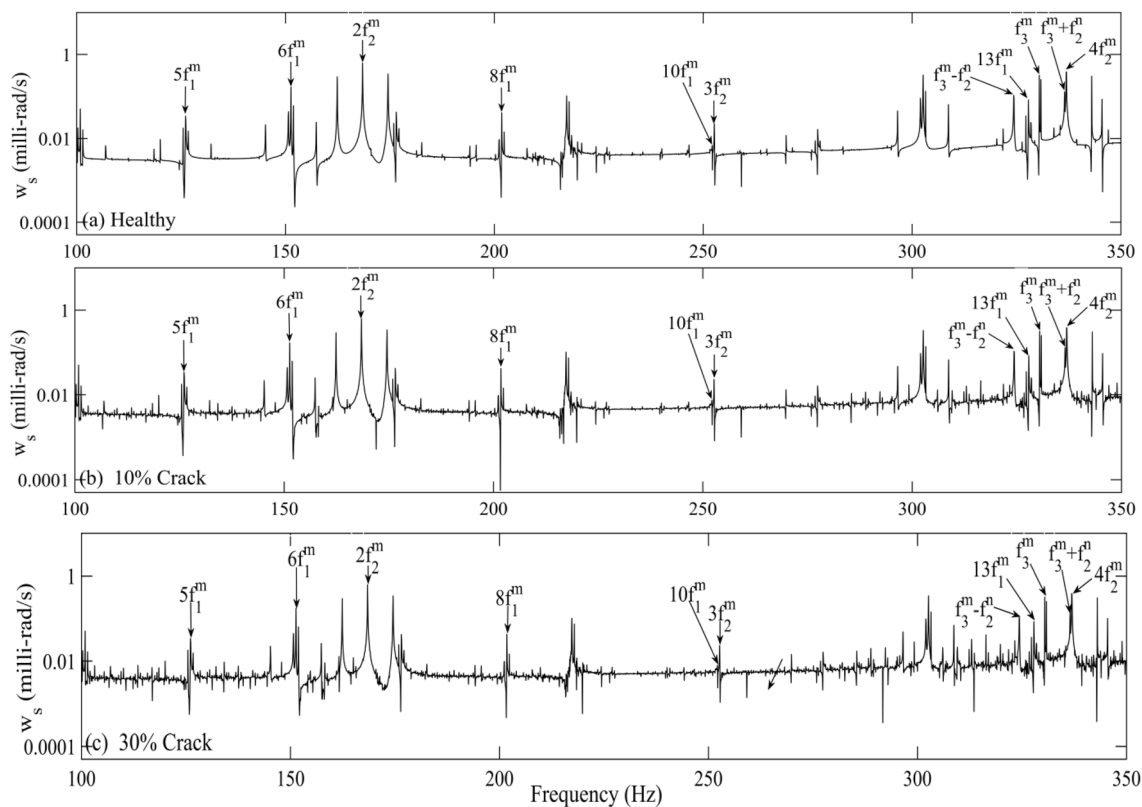
Fig. 21 Frequency spectra of speed fluctuation of the sun gear at varying crack levels assuming y-axis in logarithmic scale (0–35 Hz): **a** healthy, **b** 10% crack, and **c** 30% crack
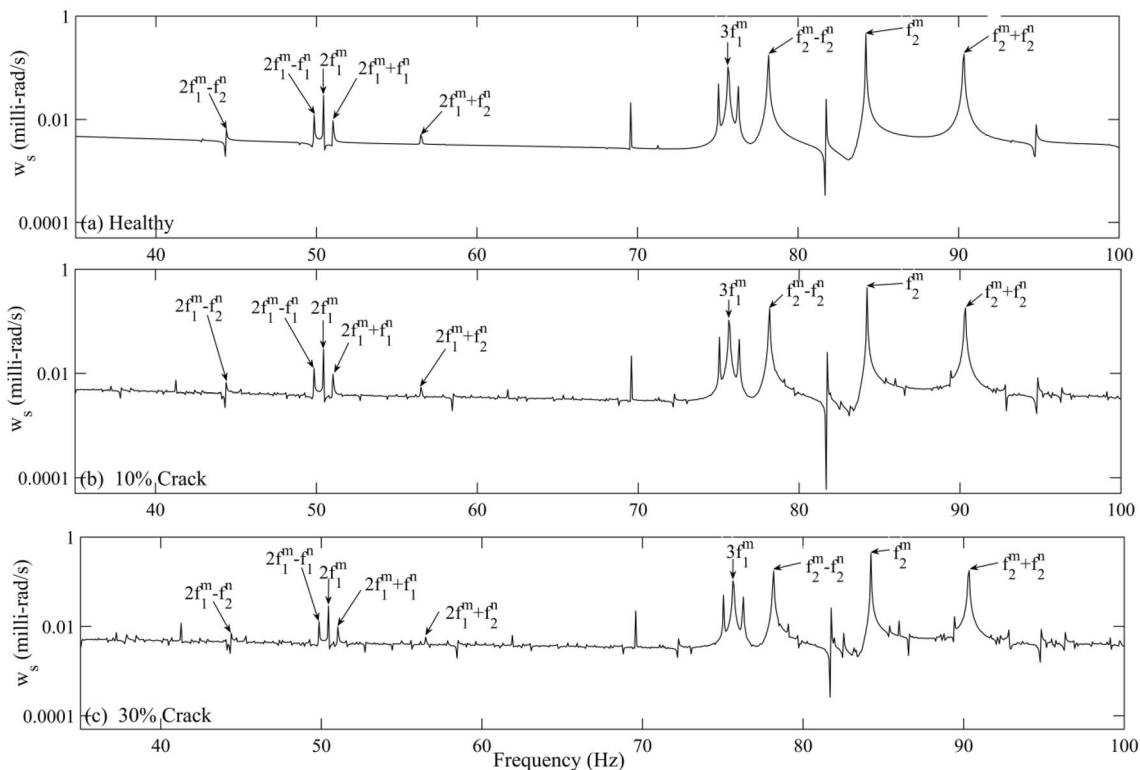
Fig. 22 Frequency spectra of speed fluctuation of the sun gear at varying crack levels assuming y-axis in logarithmic scale (35–100 Hz): **a** healthy, **b** 10% crack, and **c** 30% crack
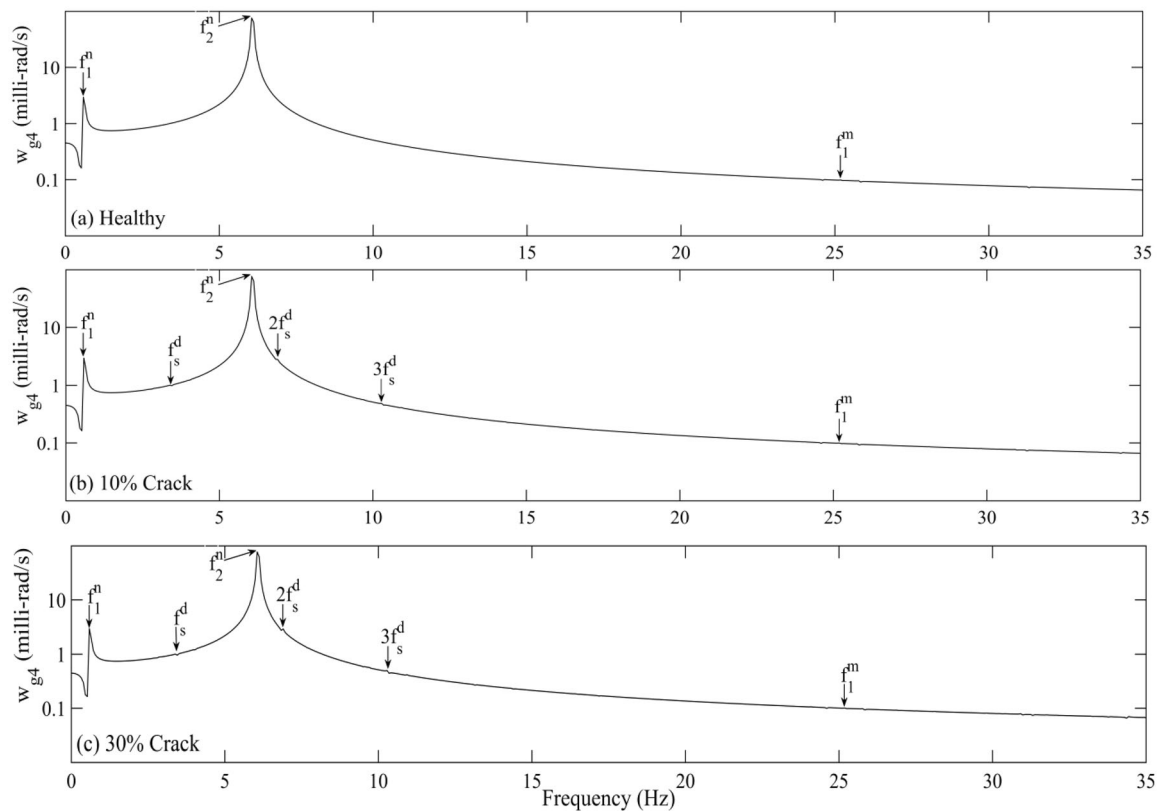
Fig. 23 Frequency spectra of speed fluctuation of the sun gear at varying crack levels assuming y-axis in logarithmic scale (100–350 Hz): **a** healthy, **b** 10% crack, and **c** 30% crack

The contact forces between gear1 and gear2 are fast Fourier transformed and plotted in the frequency spectrum in Figs. 13, 14, 15 for the healthy and defective situations. For the healthy system, the natural frequency is significantly excited; causing amplitude modulation at GMF's and their harmonics. Two sidebands are observed due to modulation along three GMF's but it is more pronounced at the first stage of mesh frequency. The modulating effect of the second natural frequency is significant at 2nd and 3rd GMF's compared to the first natural frequency. For the defective system, the fault frequency and its harmonics are excited but its modulating strength is very less at 2nd and 3rd GMF's of the second stage parallel gear trains.

Natural frequency, mesh frequency, and harmonics of mesh frequency are excited in the frequency spectrum. The 2nd natural frequency is modulating the 2nd and 3rd GMF's very well unlike 1st natural frequency. This is due to the proximity of the rotational frequency of gear trains to the system's natural frequency. With defective gears, fault

frequency and its harmonics are excited but its modulating strength to mesh frequency of third mesh frequency is less. With increasing crack level, the amplitude of f_s^d and its harmonics also increases. Besides this, amplitudes of GMFs, their harmonics with sidebands also increase with crack levels.

Torsional vibration can be accessed by speed sensors like rotary encoder and tachometer (Roy et al. 2014), which are generally attached to the shaft end. However, in a gearbox, it is very difficult to position the multiple speed sensors at a time. Taking note of these constraints, it is assumed that few sensors can be placed. Therefore, torsional vibrations are analysed at the shaft end of the sun gear of the 1st stage and gear 4 of the 3rd stage. In Figs. 21, 22, 23, the magnitude of speed fluctuation increases with the increase in the gear ratio of succeeding stages of the drivetrain system. The amplitude of fault frequency increases with the increase in the depth of crack in the sun

Fig. 24 Frequency spectra of speed fluctuation of the gear4 at varying crack levels assuming y-axis in logarithmic scale (0–35 Hz): **a** healthy, **b** 10% crack, and **c** 30% crack

gear. Contrary to this, the modulation effect of 1st natural frequency and defect frequency is minimal in the subsequent frequency spectra in Figs. 24, 25, 26. However, the modulation effect of 2nd natural frequency is more pronounced in the sidebands of 2nd and 3rd stage GMFs and their harmonics. Comparative spectral analysis is done for the un-cracked case (0% crack level) and cracked case with crack levels being 10% and 30% on tooth root of the sun gear. This can help in health monitoring of the WTDS as a preventive measure to any industrial hazard coming in.

5 Conclusions

The present mathematical model is developed to investigate the dynamics of the WTDS for constant input torque using Lagrange's formulation. This model has taken into account the analytically estimated TVMS for healthy and cracked sun gear tooth, phase shift due to angular orientation of the planets, the flexibility of the shaft, and the bearing stiffness. The Houbolt technique is applied to solve the equations of motion of the developed model numerically. The contact forces between the meshing gears and angular speeds from the sun gear and gear 4 are analysed in the frequency domain. Thus, an effective comparison is

made between healthy and defective WTDS. Frequency spectra of the healthy drivetrain show the excitation of the natural frequencies of the system, GMFs of meshing gear pairs along with sidebands and their harmonics. In the case of defective WTDS, the fault characteristic frequency and its harmonics are excited and the amplitude of these frequencies increases with increasing the depth of the crack. As well as, this frequency modulates the dynamic responses.

With this, the health diagnosis of the WTDS becomes an important aspect of a wind turbine. Detection of gear tooth crack under constant wind speed is a stepping-stone for future work. This work can be extended for the analysis of WTDS under non-stationary wind load conditions in the future. However, due to inappropriate condition monitoring of the critical components of the WT, the operational life of the WT plant has been reduced to one-fourth. This increases the cost of wind energy. As well as it demotivates the industry to invest and rely on wind energy. Hence, the modelling and analysis of the WTDS will help to develop a more accurate and reliable health diagnosis technique for the WTDS. Thus it will gradually improve the reliability, system safety, and operational life of the WTDS. Finally, the industry will look to wind energy as a secured investment for future power.
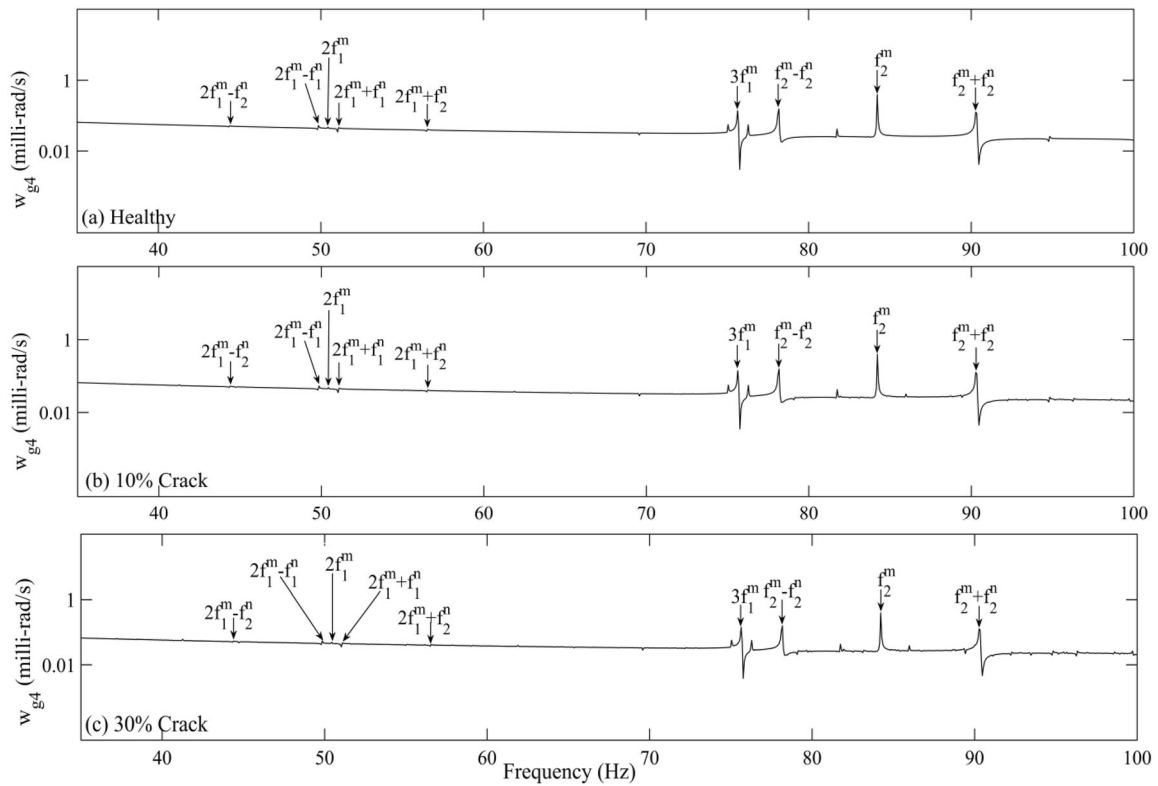
Fig. 25 Frequency spectra of speed fluctuation of the gear4 at varying crack levels assuming y-axis in logarithmic scale (35–100 Hz): **a** healthy, **b** 10% crack, and **c** 30% crack
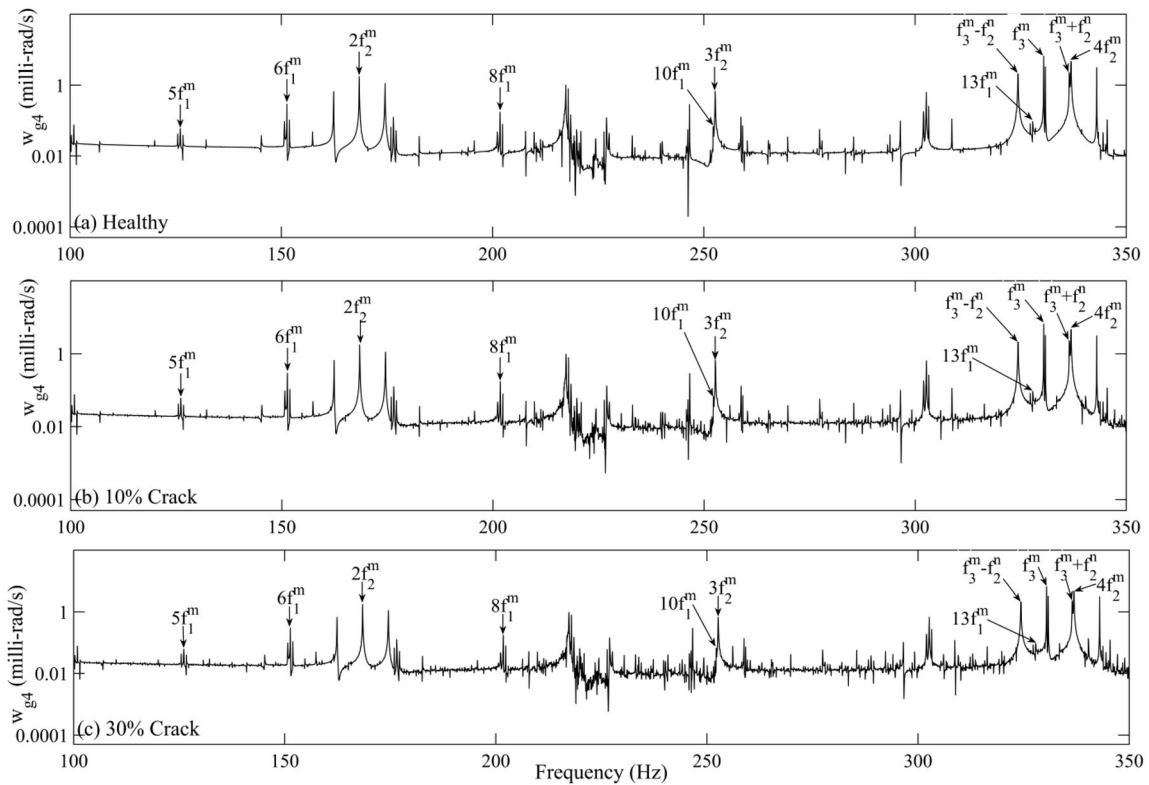
Fig. 26 Frequency spectra of speed fluctuation of gear4 at varying crack levels assuming y-axis in logarithmic scale (100–350 Hz): **a** healthy, **b** 10% crack, and **c** 30% crack

Appendix

$$
K = \begin{bmatrix}
K_{1,1} & K_{1,2} & 0 & 0 & 0 & 0 & 0 & 0 & 0 & 0 & 0 \\
K_{2,1} & K_{2,2} & K_{2,3} & K_{2,4} & K_{2,5} & K_{2,6} & 0 & 0 & 0 & 0 & 0 \\
0 & K_{3,2} & K_{3,3} & 0 & 0 & K_{3,6} & 0 & 0 & 0 & 0 & 0 \\
0 & K_{4,2} & 0 & K_{4,4} & 0 & K_{4,6} & 0 & 0 & 0 & 0 & 0 \\
0 & K_{5,2} & 0 & 0 & K_{5,5} & K_{5,6} & 0 & 0 & 0 & 0 & 0 \\
0 & K_{6,2} & K_{6,3} & K_{6,4} & K_{6,5} & K_{6,6} & K_{6,7} & 0 & 0 & 0 & 0 \\
0 & 0 & 0 & 0 & 0 & -k_{t2} & K_{7,7} & K_{7,8} & 0 & 0 & 0 \\
0 & 0 & 0 & 0 & 0 & 0 & K_{8,7} & K_{8,8} & K_{8,9} & 0 & 0 \\
0 & 0 & 0 & 0 & 0 & 0 & 0 & K_{9,8} & K_{9,9} & K_{9,10} & 0 \\
0 & 0 & 0 & 0 & 0 & 0 & 0 & 0 & K_{10,9} & K_{10,10} & -k_{t3} \\
0 & 0 & 0 & 0 & 0 & 0 & 0 & 0 & 0 & -k_{t3} & k_{t3}
\end{bmatrix}
$$

where, $K_{2,2} = k_{t1} + (k_{rp1} + k_{rp2} + k_{rp3})R_r^2 + (k_{sp1} + k_{sp2} + k_{sp3})R_s^2 + k_{bc}$, $K_{7,7} = (k_{t2} + k_{g12}R_1^2)$, $K_{6,7} = K_{7,6} = -k_{t2}$, $K_{1,2} = K_{2,1} = -k_{t2}$, $K_{8,9} = K_{9,8} = -k_{t2}$, $K_{10,11} = K_{11,10} = -k_{t3}$, $K_{2,3} = K_{3,2} = (k_{rp1}R_pR_r - k_{sp1}R_pR_s)$, $K_{6,6} = k_{t2} + (k_{sp1} + k_{sp2} + k_{sp3})R_s^2 + k_{bs}$, $K_{10,10} = (k_{t3} + k_{g34}R_4^2)$, $K_{2,4} = K_{4,2} = (k_{rp2}R_pR_r - k_{sp2}R_pR_s)$, $K_{1,1} = k_{t2}$, $K_{11,11} = k_{t3}$, $K_{2,5} = K_{5,2} = (k_{rp3}R\,pR_r - k_{sp3}R_p\,R_s)$, $K_{2,6} = K_{6,2} = -(k_{sp1} + k_{sp2} + k_{sp3})R_s^2$, $K_{5,6} = K_{6,5} = k_{sp3}R_pR_s$, $K_{9,9} = (k_{t3} + k_{g34}R_3^2)$, $K_{4,4} = (k_{rp2} + k_{sp2})R_p^2$, $K_{7,8} = K_{8,7} = (k_{g12}R_{g1}R_{g2})$, $K_{8,8} = (k_{t2} + k_{g12}R_2^2)$, $K_{5,5} = (k_{rp3} + k_{sp3})R_p^2$, $K_{3,6} = K_{6,3} = k_{sp1}R_pR_s$, $K_{9,10} = K_{10,9} = (k_{g34}R_{g3}R_{g4})$, $K_{4,6} = K_{6,4} = k_{sp2}R_pR_s$, $K_{3,3} = (k_{rp1} + k_{sp1})R_p^2$

$$
\theta = \begin{bmatrix} \theta_{rot} & \theta_c & \theta_{cp1} & \theta_{cp2} & \theta_{cp3} & \theta_s & \theta_{g1} & \theta_{g2} & \theta_{g3} & \theta_{g4} & \theta_{gen} \end{bmatrix}^T
$$

$$
\Gamma = \begin{bmatrix} \Gamma_{rot} & 0 & 0 & 0 & 0 & 0 & 0 & 0 & 0 & 0 & \Gamma_{gen} \end{bmatrix}^T
$$

$$
M = \begin{bmatrix}
J_{rot} & 0 & 0 & 0 & 0 & 0 & 0 & 0 & 0 & 0 & 0 \\
0 & J_c + 3J_p + 3mR_c^2 & J_p & J_p & J_p & 0 & 0 & 0 & 0 & 0 & 0 \\
0 & J_p & J_p & 0 & 0 & 0 & 0 & 0 & 0 & 0 & 0 \\
0 & J_p & 0 & J_p & 0 & 0 & 0 & 0 & 0 & 0 & 0 \\
0 & J_p & 0 & 0 & J_p & 0 & 0 & 0 & 0 & 0 & 0 \\
0 & 0 & 0 & 0 & 0 & J_s & 0 & 0 & 0 & 0 & 0 \\
0 & 0 & 0 & 0 & 0 & 0 & J_{g1} & 0 & 0 & 0 & 0 \\
0 & 0 & 0 & 0 & 0 & 0 & 0 & J_{g2} & 0 & 0 & 0 \\
0 & 0 & 0 & 0 & 0 & 0 & 0 & 0 & J_{g3} & 0 & 0 \\
0 & 0 & 0 & 0 & 0 & 0 & 0 & 0 & 0 & J_{g4} & 0 \\
0 & 0 & 0 & 0 & 0 & 0 & 0 & 0 & 0 & 0 & J_{gen}
\end{bmatrix}
$$

References

Bhattacharya A, Dan PK (2014) Recent trend in condition monitoring for equipment fault diagnosis. Int J Syst Assur Eng Manage 5(3):230–244. https://doi.org/10.1007/s13198-013-0151-z

Cao Z, Qian H, Zareipour Z, Huang Z, Zhang F (2019) Fault diagnosis of wind turbine gearbox based on deep bi-directional long short-term memory under time-varying non-stationary operating conditions. IEEE Access 7:55219–155228. https://doi.org/10.1109/ACCESS.2017

Chaari F, Fakhfakh T, Haddar M (2006) Analytical investigation on the effect of gear teeth faults on the dynamic response of a planetary gear set. Noise Vib Worldw 37:9–15. https://doi.org/10.1260/095745606778600857

Chaari F, Fakhfakh T, Haddar M (2009) Analytical modelling of spur gear tooth crack and influence on gear mesh stiffness. Eur J Mech A/Solids 28:461–468. https://doi.org/10.1016/j.euromechsol.2008.07.007

Chen X, Feng Z (2016) Iterative generalized time–frequency reassignment for planetary gearbox fault diagnosis under non-stationary conditions. Mech Syst Signal Process 80:429–444

Chen Z, Shao Y (2011) Dynamic simulation of spur gear with tooth root crack propagating along tooth width and crack depth. Eng Fail Anal 18:2149–2164. https://doi.org/10.1016/j.engfailanal.2011.07.006

Chen Z, Shao Y (2013a) Dynamic features of a planetary gear system with tooth crack under different sizes and inclination angles. J Vib Acoust 135:031004/1–12. https://doi.org/10.1115/1.4023300

Chen Z, Shao Y (2013b) Dynamic simulation of planetary gear with tooth root crack in ring gear. Eng Fail Anal 31:8–18. https://doi.org/10.1016/j.engfailanal.2013.01.012

Dewangan P, Parey A, Hammami A, Chaari F, Haddar M (2020) Damage detection in wind turbine gearbox using modal strain energy. Eng Fail Anal 107:104228

Dewangan P, Parey A, Hammami A, Chaari F, Haddar M (2022) Dynamic characteristics of a wind turbine gearbox with amplitude modulation and gravity effect: theoretical and experimental investigation. Mech Mach Theory 167:104468

Feng Z, Zhu W, Zhang D (2019) Time-frequency demodulation analysis via Vold-Kalman filter for wind turbine planetary gearbox fault diagnosis under nonstationary speeds. Mech Syst Sig Process 12:93–109. https://doi.org/10.1016/j.ymssp.2019.03.036

Gasch R, Twele J (2011) Wind power plants: fundamentals, design, construction and operation. Springer-Verlag, Berlin Heidelberg

Girsang IP, Dhupia JS, Muljadi E, Singh M, Pao LY (2014) Gearbox and drivetrain models to study dynamic effects of modern wind turbines. IEEE Trans Ind Appl 50(6):3777–3786

He G, Ding K, Li W, Li Y (2017) Frequency response model and mechanism for wind turbine planetary gear train vibration analysis. IET Renew Power Gener 11(4):425–432. https://doi.org/10.1049/iet-rpg.2016.0236

Helsen J, Vanhollebeke F, Coninck FD, Vandepitte D, Desmet W (2011a) Insights of wind turbine drive train dynamics gathered by validating advanced models on a newly developed 13.2 MW dynamically controlled test rig. Mechatronics 21:737–752. https://doi.org/10.1016/j.mechatronics.2010.11.005

Helsen J, Vanhollebeke F, Marrant B, Vandepitte D, Desmet W (2011b) Multibody modelling of varying complexity for modal behaviour analysis of wind turbine gearboxes. Renew Energy 36:3098–3113. https://doi.org/10.1016/j.renene.2011.03.023

Hong L, Dhupia JS, Sheng S (2014) An explanation of frequency features enabling detection of faults in equally spaced planetary gearbox. Mech Mach Theory 73:169–183. https://doi.org/10.1016/j.mechmachtheory.2013.10.014

Howard I, Jia SX, Wang JD (2001) The dynamic modelling of a spur gear in mesh including friction and a crack. Mech Syst Signal Process 15:831–853

IRENA (2021) Renewable Capacity Statistics 2021. *International Renewable Energy Agency*, Abu Dhabi, 1–64. https://www.irena.org/publications/2021/March/Renewable-Capacity-Statistics-2021

Lei YG, Lin J, Zuo MJ, He Z (2014) Condition monitoring and fault diagnosis of planetary gearboxes: a review. Measurement 48:292–330

Liang X, Zue MJ, Pandey M (2014) Analytically evaluating the influence of crack on the mesh stiffness of a planetary gear set. Mech Mach Theory 76:20–38. https://doi.org/10.1016/j.mechmachtheory.2014.02.001

Liang X, Zuo MJ, Hoseini MR (2015) Vibration signal modeling of a planetary gear set for tooth crack detection. Eng Fail Anal 48:185–200. https://doi.org/10.1016/j.engfailanal.2014.11.015

Liu X, Yang Y, Zhang J (2017) Effects of tooth-crack-induced mesh stiffness on fault signals of a planetary gear train. Proc Comput Sci 109:785–792. https://doi.org/10.1016/j.procs.2017.05.324

Liu X, Yang Y, Zhang J (2018) Resultant vibration signal based fault diagnosis of single stage planetary gear train with an incipient tooth crack on the sun gear. Renew Energy 122:65–79. https://doi.org/10.1016/j.renene.2018.01.072

MNRE-GOI (2021) Annual Report 2021. *Ministry of New and Renewable Energy- Government of India*, 1–180. https://mnre.gov.in/img/documents/uploads/file_f-1618564141288.pdf

Ma H, Zeng J, Feng R, Pang X, Wang Q, Wen B (2015) Review on dynamics of cracked gear systems. Eng Fail Anal 55:224–245. https://doi.org/10.1016/j.engfailanal.2015.06.004

Pandya Y, Parey A (2013) Experimental investigation of spur gear tooth mesh stiffness in the presence of crack using photoelasticity technique. Eng Fail Anal 34:488–500. https://doi.org/10.1016/j.engfailanal.2013.07.005

Parker RG, Lin J (2004) Mesh phasing relationships in planetary and epicyclic gears. J Mech Des 126:365–370. https://doi.org/10.1115/1.166789

Peeters JLM, Vandepitte D, Sas P (2006a) Analysis of internal drive train dynamics in a wind turbine. Wind Energy 9:141–161. https://doi.org/10.1002/we.173

Peeters JLM, Vandepitte D, Sas P (2006) Structural analysis of a wind turbine and its drive train using the flexible multibody simulation technique. In: Proceedings of ISMA rotating machinery: dynamics. Leuven, Belgium, pp 3665–3680

Qin D, Wang J, Lim TC (2009) Flexible multibody dynamic modeling of a horizontal wind turbine drivetrain system. J Mech Des 131:114501-1-114501–8

Raghuwanshi NK, Parey A (2016) Experimental measurement of gear mesh stiffness of cracked spur gear by strain gauge technique. Measurement 86:266–275. https://doi.org/10.1016/j.measurement.2016.03.001

Rao SS (2011) Mechanical Vibrations, 5th edn. Pearson Prentice Hall, New Jersey

Roy SK, Mohanty AR, Kumar CS (2014) Fault detection in a multistage gearbox by time synchronous averaging of the instantaneous angular speed. J Vib Control 22(2):468–480

Shi W, Kim CW, Chung CW, Park HC (2013) Dynamic modelling and analysis of a wind turbine drive train using the torsional dynamic model. Int J Precis Eng Manuf 14:153–159. https://doi.org/10.1007/s12541-013-0021-2

Shi W, Park HC, Na S, Song J, Ma S, Kim CW (2014) Dynamic analysis of three-dimensional drive train system of wind turbine. Int J Precis Eng Manuf 15:1351–1357. https://doi.org/10.1007/s12541-014-0476-9

Singh S, Baglee D, Michael K, Galar D (2015) Developing RCM strategy for wind turbines utilizing e-condition monitoring. Int J Syst Assur Eng Manage 6:150–156. https://doi.org/10.1007/s13198-014-0259-9

Srikanth P, Sekhar AS (2013) Dynamic analysis of drive train of a fixed speed wind turbine. 20th Int. Congr Sound Vib 2013:42–49

Srikanth P, Sekhar AS (2015) Dynamic analysis of wind turbine drive train subjected to nonstationary wind load excitation. J Mech Eng Sci 229:429–446. https://doi.org/10.1177/0954406214536547

Srikanth P, Sekhar AS (2016) Wind turbine drive train dynamic characterization through Vibration and Torque signals. Mech Mach Theory 98:2–20. https://doi.org/10.1016/j.mechmachtheory.2015.11.013

Tan J, Zhu C, Song C, Li Y, Xu X (2019b) Dynamic modeling and analysis of wind turbine drivetrain considering platform motion. Mech Mach Theory 140:781–808. https://doi.org/10.1016/j.mechmachtheory.2019.06.026

Tan J, Zhu C, Song C, Xu X (2019a) Study on the dynamic modeling and natural characteristics of wind turbine drivetrain considering electromagnetic stiffness. Mech Mach Theory 134:541–561. https://doi.org/10.1016/j.mechmachtheory.2019.01.015

Todorov M, Dobrev I, Massouh F (2009) Analysis of torsional oscillation of the drive train in horizontal-axis wind turbine. In: Electro motion 2009-EPE chapter electric drives joint symposium, Lille, France, pp 56–62

Viadero F, Fernández A, Iglesias M, de Juan A, Liaño E, Serna MA (2014) Non-stationary dynamic analysis of a wind turbine power drivetrain: offshore considerations. Appl Acoust 77:204–211. https://doi.org/10.1016/j.apacoust.2013.10.006

Wang T, Chu F, Han Q (2017) Fault diagnosis of wind turbine planetary ring gear via a meshing resonance based filtering algorithm. ISA Trans 67:173–182. https://doi.org/10.1016/j.isatra.2016.11.008

Wang T, Han Q, Chu F, Feng Z (2019) Vibration based condition monitoring and fault diagnosis of wind turbine planetary gearbox: A review. Mech Syst Signal Process 126:662–685. https://doi.org/10.1016/j.ymssp.2019.02.051

Wang J, Howard I (2004) The torsional stiffness of involute spur gears. Proc Inst Mech Eng C J Mech Eng Sci 218:131–142. https://doi.org/10.1243/095440604322787009

Wang L, Shao Y, Cao Z (2018) Optimal demodulation sub-band for sun gear crack fault diagnosis in planetary gearbox. Measurement 125:554–563. https://doi.org/10.1016/j.measurement.2018.05.023

Wang W, Wu S (2011) Nonlinear dynamic modelling and numerical simulation of the wind turbine's gear train. In: Proceedings of the international conference on electrical and control engineering (ICECE). Yichang, China, pp 2385–2389

Xing Y, Moan T (2013) Multi-body modelling and analysis of a planet carrier in a wind turbine gearbox. Wind Energy 16:1067–1089

Yoon J, He D, Hecke BV, Nostrand TJ, Zhu J, Bechhoefer E (2016) Vibration based wind turbine planetary gearbox fault diagnosis using spectral averaging. Wind Energy 19:1733–1747. https://doi.org/10.1002/we.1940

Zhai H, Zhu C, Song C, Liu H, Bai H (2016) Influences of carrier assembly errors on the dynamic characteristics for wind turbine gearbox. Mech Mach Theory 103:138–147. https://doi.org/10.1016/j.mechmachtheory.2016.04.015

Zhu C, Chen S, Liu H, Huang H, Li G, Ma F (2014) Dynamic analysis of the drive train of a wind turbine based upon the measured load spectrum. J Mech Sci Technol 28:2033–2040. https://doi.org/10.1007/s12206-014-0403-0